AGU PUBLICATIONS

Water Resources Research

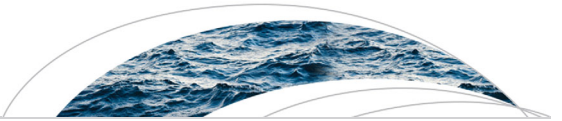

RESEARCH ARTICLE

10.1002/2015WR018451

Analytical and numerical investigations of spontaneous imbibition in porous media

Hasan A. Nooruddin[1] and Martin J. Blunt[1]

[1]Department of Earth Science and Engineering, Imperial College London, UK

Key Points:
- Spontaneous imbibition
- Immiscible fluid displacements
- Fractional flow

Correspondence to:
H. A. Nooruddin,
h.nourdeen14@imperial.ac.uk or
hasan.a.nooruddin@gmail.com

Citation:
Nooruddin, H. A., and M. J. Blunt (2016), Analytical and numerical investigations of spontaneous imbibition in porous media, *Water Resour. Res.*, *52*, doi:10.1002/2015WR018451.

Received 2 DEC 2015
Accepted 23 AUG 2016
Accepted article online 25 AUG 2016

Abstract We present semianalytical solutions for cocurrent displacements with some degree of countercurrent flow. The solution assumes a one-dimensional horizontal displacement of two immiscible incompressible fluids with arbitrary viscosities and saturation-dependent relative permeability and capillary pressures. We address the impact of the system length on the degree of countercurrent flow when there is no pressure drop in the nonwetting phase across the system, assuming negligible capillary back pressure at the inlet boundary of the system. It is shown that in such displacements, the fractional flow can be used to determine a critical water saturation, from which regions of both cocurrent and countercurrent flow are identified. This critical saturation changes with time as the saturation front moves into the porous medium. Furthermore, the saturation profile in the approach presented here is not necessarily a function of distance divided by the square root of time. We also present approximate solutions using a perturbative approach, which is valid for a wide range of flow conditions. This approach requires less computational power and is much easier to implement than the implicit integral solutions used in previous work. Finally, a comprehensive comparison between analytical and numerical solutions is presented. Numerical computations are performed using traditional finite-difference formulations and convergence analysis shows a generally slow convergence rate for water imbibition rates and saturation profiles. This suggests that most coarsely gridded simulations give a poor estimate of imbibition rates, while demonstrating the value of these analytical solutions as benchmarks for numerical studies, complementing Buckley-Leverett analysis.

1. Introduction

The unsteady flow of immiscible fluids in porous media is of great importance in many areas of research and industrial application. The simultaneous flow of two or more immiscible fluids often occurs in the porous rocks of hydrocarbon reservoirs. The displacement of oil by water is widely applied to maintain reservoir pressure and increase oil recovery.

Most carbonate reservoirs, which contain more than 60% of the world's conventional oil reserves [*Beydoun*, 1998; *Montaron*, 2008], are naturally fractured [*Agada et al*., 2013; *Mou et al*., 2012]. In naturally fractured reservoirs, capillary forces control the recovery process by allowing the movement of immiscible fluids between matrix-blocks and the fractures. This process is called spontaneous imbibition [*Morrow and Mason*, 2001; *Mason and Morrow*, 2013], and occurs in two forms: countercurrent and cocurrent flow. Under countercurrent displacements, the wetting and nonwetting fluids flow in opposite directions but with identical flow rates; the total flow rate is zero. This is achieved in linear systems by allowing the exchange of fluids across the inlet boundary while the other boundary is closed. In cocurrent flow, however, flow is allowed through both inlet and outlet boundaries, such that there exists a net total flow rate in the flow direction of the wetting fluid. In some cases of cocurrent flow, however, some degree of countercurrent flow of the nonwetting fluid is encountered across the inlet boundary. This is simply because the nonwetting phase may easily escape back through the inlet, particularly when the front of wetting phase has only advanced a short distance into the rock. This displacement process can be replicated in the laboratory by exposing one of the two faces of the core to oil and the other face to water [*Haugen et al*., 2014; *Mason and Morrow*, 2013; *Ruth et al*., 2015]. This backflow of oil can be prevented by using a semipermeable membrane that is permeable to the wetting phase only [*Chen et al*., 1992]. In such cases, the fluids are forced to flow in one direction and the displacement is said to be unidirectional [*Mason and Morrow*, 2013].

Numerical simulations are routinely conducted to evaluate the performance of hydrocarbon reservoirs under various operational conditions. To ensure the reliability of these numerical solvers, a validation

© 2016. The Authors.
This is an open access article under the terms of the Creative Commons Attribution-NonCommercial-NoDerivs License, which permits use and distribution in any medium, provided the original work is properly cited, the use is non-commercial and no modifications or adaptations are made.

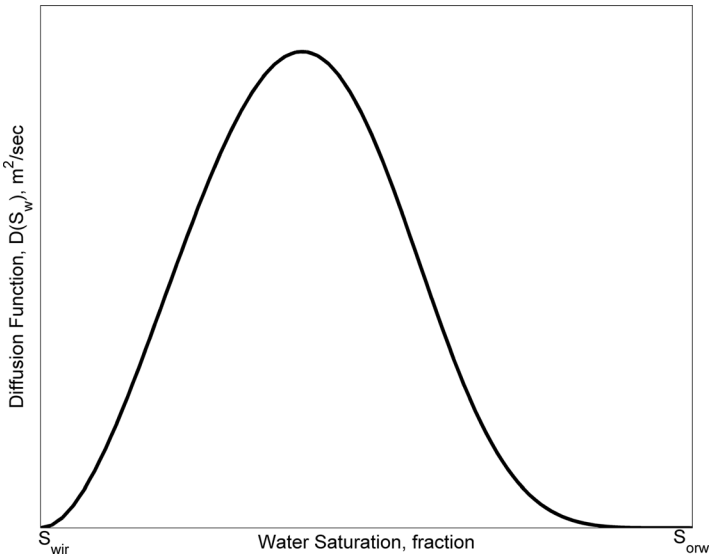

Figure 1. An illustration of the characteristic of the capillary diffusion function $D(S_w)$ with water saturation in strongly water-wet media.

process is usually performed. The best method is to compare the numerical results against nontrivial analytical solutions. Developing solutions for capillary-driven flow, either numerically or analytically, is considered a difficult problem due primarily to the nonlinearity in the original two-phase flow equations. Analytical solutions were developed by *McWhorter and Sunada* [1990] for spontaneous imbibition under counter and cocurrent displacements in linear and radial systems. Unlike other solutions that assume specific functional forms of the relative permeabilities and capillary pressures [*Fokas and Yortsos*, 1982; *Kashchiev et al*., 2003; *Chen et al*., 1988], the saturation-dependent functions in the *McWhorter and Sunada* solution are completely arbitrary.

The main assumption in the *McWhorter and Sunada* solution is that the imbibition rate, for both co and countercurrent flow, is inversely proportional to the square root of time. The authors, however, used this assumption as a forced boundary condition that is externally applied, rather than an inherent physical characteristic of the system. *Schmid et al*. [2011] showed that this boundary condition is indeed correct for imbibition problems. We will show, however, that this is only true in countercurrent and unidirectional flow systems, and does not necessarily apply to the general case of cocurrent flow, when some degree of countercurrent flow is allowed during the displacement.

In this paper, we present a new analytical methodology to solve for cocurrent displacements with some degree of countercurrent flow. We also present a comprehensive investigation of spontaneous imbibition processes in porous rocks both numerically and analytically. In addition, we present a simplified solution using the perturbation theory that can be easily implemented without the need to use the implicit integral solutions.

2. Governing Equations

The partial differential equation (PDE) that describes horizontal, immiscible, and incompressible two-phase flow in porous media is given by

$$\frac{\partial}{\partial x}\left(D(S_w)\frac{\partial S_w(x,t)}{\partial x}\right)-q_t(t)\frac{df_w(S_w)}{dS_w}\frac{\partial S_w(x,t)}{\partial x}=\phi\frac{\partial S_w(x,t)}{\partial t}, \tag{1}$$

where q_t is the total volume flux, S_w is the saturation of the wetting phase, which in this case is water, x is distance, t is time, and ϕ is porosity. The saturation-dependent functions $f_w(S_w)$ and $D(S_w)$ are given by

$$f_w(S_w)=\frac{1}{1+\frac{\mu_w k_{ro}(S_w)}{\mu_o k_{rw}(S_w)}}, \tag{2}$$

$$D(S_w)=-\frac{k}{\mu_o}k_{ro}(S_w)f_w(S_w)\frac{dp_c(S_w)}{dS_w}, \tag{3}$$

where D is the capillary dispersion function, f_w is the water fractional flow for viscous-dominated displacements, μ_w is the water viscosity, μ_o is the oil viscosity, k_{rw} is the water relative permeability, k_{ro} is the oil

relative permeability, p_c is the capillary pressure for imbibition, and k is the absolute permeability. For physically meaningful relative permeabilities and capillary pressures in a strongly water-wet environment, D is a bell-shaped function of water saturation (Figure 1). The negative sign is introduced since $p_c'(S_w)$ is always negative.

The partial differential equation in equation (1) is developed by combining the material balance equation;

$$-\frac{\partial q_w(x,t)}{\partial x}=\phi\frac{\partial S_w(x,t)}{\partial t}\,, \tag{4}$$

with the expression of water flux given as

$$q_w(x,t)=q_t(t)f_w(S_w)-D(S_w)\frac{\partial S_w(x,t)}{\partial x}\,. \tag{5}$$

In 1-D systems, q_t is constant in space but not necessarily in time. In countercurrent displacements, q_t vanishes.

3. Analytical Solution

An exact solution for equation (1) is derived by using the fractional flow concept [*McWhorter et al*., 1971; *McWhorter and Sunada*, 1990] which is valid for arbitrary saturation-dependent functions. The key idea is to express the water flux in equation (5) as a function of fractional flow $F_w(S_w)$ according to the following relationship:

$$q_w(x,t)=q_w(0,t)\,F_w(x,t)\,. \tag{6}$$

The fractional flow function used in equation (6) is not the same as the conventional fractional flow, f_w, since the water flux here is normalized to the water flux at $x=0$, as compared to the total flux used in the conventional definition. Consequently, $F_w(S_w)$ in equation (6) will always be bounded between zero and one. The function $q_w(0,t)$, evaluated at the inlet boundary, is assumed to be inversely proportional to $\sqrt{t}$, which is not necessarily valid, as will be shown later, for all flow conditions, but rather for a few limited cases. If we make this assumption on the time-dependence of q_{x0}, we may write

$$q_{x0}=q_w(0,t)=\frac{A}{\sqrt{t}}\,, \tag{7}$$

where A is the imbibition rate parameter, in units of distance per square root of time, that depends on a preset water saturation at the inlet boundary, S_{x0}. The solution involves using the variable transformations $\lambda=x\,t^{-1/2}$ on the material balance equation, equation (4), with the flux definitions in equations (6) and (7) to obtain

$$x(t,S_w)=\frac{2A(1-f_iR)}{\phi}F_w'(S_w)\sqrt{t}\,, \tag{8}$$

where f_i is the viscous-dominated fractional flow, defined in equation (2), evaluated at initial water saturation, S_i while R is the ratio between the total rate to the water imbibition rate, q_t/q_{x0}.

From equation (8), it can be seen that the solution requires finding $F_w'(S_w)$ and A, which can be obtained by solving the following ordinary differential equation:

$$\frac{\mathrm{d}^2F_w}{\mathrm{d}S_w^2}=\frac{-\phi}{2A^2(1-f_iR)^2}\frac{D}{F_w-f_n}\,, \tag{9}$$

subject to

$$S_w(0,t)=S_{x0}\qquad F_w(S_{x0})=1\,, \tag{10}$$

$$S_w(\infty,t)=S_i\qquad F_w(S_i)=0\,, \tag{11}$$

where f_n is the normalized viscous-dominated fraction flow defined by

$$f_n = \frac{R(f_w - f_i)}{1 - f_i R}. \tag{12}$$

Solving equation (9) for F_w with the boundary conditions defined in equations (10) and (11) yields

$$F_w(S_w) = 1 - \left(\int_{S_w}^{S_{x0}} \frac{(\beta - S_w)D(\beta)}{F_w(\beta) - f_n(\beta)} d\beta \right) \times \left(\int_{S_i}^{S_{x0}} \frac{(\beta - S_i)D(\beta)}{F_w(\beta) - f_n(\beta)} d\beta \right)^{-1}, \tag{13}$$

and hence

$$F'_w(S_w) = \left(\int_{S_w}^{S_{x0}} \frac{D(\beta)}{F_w(\beta) - f_n(\beta)} d\beta \right) \times \left(\int_{S_i}^{S_{x0}} \frac{(\beta - S_i)D(\beta)}{F_w(\beta) - f_n(\beta)} d\beta \right)^{-1}, \tag{14}$$

$$A = \left(\frac{\phi}{2(1 - f_i R)^2} \int_{S_i}^{S_{x0}} \frac{(\beta - S_i)D(\beta)}{F_w(\beta) - f_n(\beta)} d\beta \right)^{1/2}. \tag{15}$$

The mathematical derivations of the nonlinear differential equation in equation (9) and its solutions in equations (13), (14), and (15) follow the approach of *McWhorter and Sunada* [1990] and *Schmid et al.* [2011]. The solution is attained by first solving for $F_w(S_w)$ from the implicit integral expression in equation (13). Then, $F'_w(S_w)$ and A can be computed from equations (14) and (15) and plugged into equation (8) to determine the distance profile. The implicit integral solutions require using an iterative scheme. The computations are carried out by a first assumption of $F_w(S_w) = 1$ for all values of S_w inside the definite integrals on the right side of equation (13), *Schmid et al.* [2011]. The updated $F_w(S_w)$ on the left side can then be used for the next iteration. This process continues until the difference between the updated and previous values is less than a prescribed error tolerance. It is observed that the implicit solution converges rapidly for countercurrent displacements ($R = 0$ and hence, $f_n(S_w) = 0$) within 3–4 iterations.

Other than the solution procedure presented by *McWhorter and Sunada* [1990], many algorithms have been proposed for an improved and stable performance [*Fučík et al.*, 2007; *Bjørnarå and Mathias*, 2013]. For example, *Bjørnarå and Mathias* [2013] presented an approach to obtain the solutions without using the implicit integrals in equations (13), (14) and (15). This was achieved by solving the ordinary differential equation (9) using a pseudospectral differentiation matrix. This approach is as accurate as the implicit integral solutions presented by *McWhorter and Sunada* [1990], but it is much faster and more robust, especially for cocurrent displacements where the implicit integral solutions may fail to converge.

For cocurrent displacements with no countercurrent flow allowed at the inlet boundary ($R = 1$), convergence problems might arise, especially for high mobility ratios. This can be observed clearly from equation (13) since the integrand becomes improper with a singularity at $F_w(S_w) = f_n(S_w)$. The range of integration within which this singularity is encountered increases as the mobility ratio increases. This is illustrated graphically in Figure 2 where $F_w(S_w)$ is plotted as a function of S_w for countercurrent and cocurrent flow using a high oil-to-water viscosity ratio. The saturation range for which $F_w(S_w) \approx f_n(S_w)$ is large as compared with low mobility ratios where a typical $f_n(S_w)$ takes a different shape. The curve becomes mainly concave upward, approaching S_{x0} at higher slopes with an inflection point. It is also demonstrated from the graph that the cocurrent fractional flow is bounded between those of countercurrent and normalized viscous-dominated flow. However, this solution is not valid for cocurrent displacements with some degree of countercurrent flow. For this flow process, *Haugen et al.* [2014] presented a simple mathematical model that assumes a piston-like displacement. We will present, however, a more rigorous mathematical treatment of the problem leading to a better description of the system.

3.1. Cocurrent Displacement With Some Degree of Countercurrent Flow

The solution for countercurrent imbibition is obtained by setting the parameter $R = 0$ since $q_t = 0$, while for cocurrent flow, $q_t = q_{x0}$ and hence $R = 1$. The latter condition, however, does not apply when there is some degree of countercurrent flow [*Chen et al.*, 1992]. For such systems, we propose a new method to obtain the solution. The key idea is that R, which controls explicitly the degree of countercurrent flow in the system,

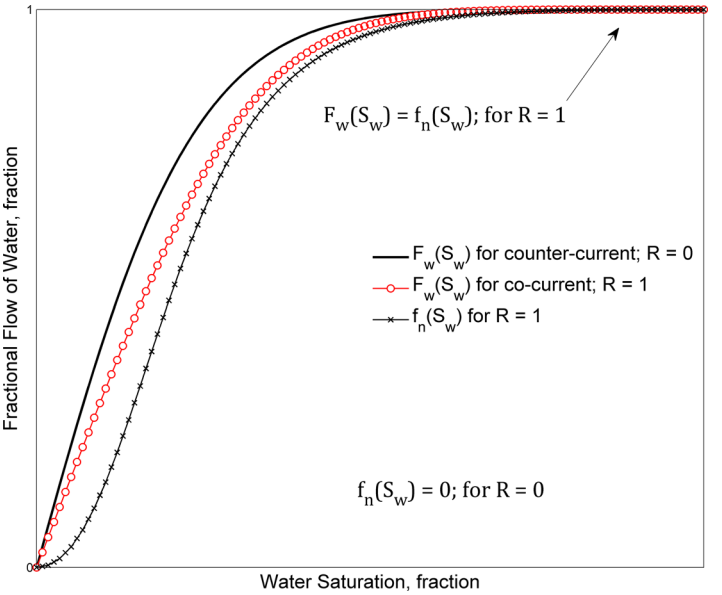

Figure 2. The characteristics of the fractional flow function F_w with S_w for countercurrent ($R = 0$) and the unidirectional cocurrent ($R = 0$) flow. For countercurrent flow, f_n becomes 0 and the implicit integral solution, equation (13), converges rapidly. For unidirectional cocurrent flow, however, $f_n = f_w$ and the integrand in equation (13) becomes improper near S_{x0}, since $F_w = f_n$.

becomes intermediate between zero and one since $q_t < q_{x0}$. Using the original solution in equation (13), $F_w(S_w)$ can be computed implicitly for any value of R. From the solution, a critical water saturation, S^*, can be identified corresponding to $F_w(S^*) = R$, at which $q_t(x^*) = q_w(x^*)$. Moreover, a region of countercurrent flow takes place between S_{x0} and S^* while cocurrent flow occurs for $S_i < S_w < S^*$. This can be deduced from the definition of $R = q_t/q_{x0}$ and the unconventional definition of fractional flow $F_w = q_w/q_{x0}$. A schematic illustrating this concept is shown in Figures 3 and 4. Consequently, R becomes an unknown parameter to be identified. However, another source of information is needed. This idea is explored further below.

In finite domains, countercurrent flow can be achieved either by applying a no-flow boundary, or imposing a constant pressure boundary $p_o(L)$ at $x = L$. For cocurrent imbibition with some countercurrent flow, however, the pressure profile takes a bell-shaped curve with a maximum pressure, p_o^*, that corresponds to the critical saturation point, S^*. In such systems, the oil pressure at the inlet and outlet boundaries is the same before the saturation front reaches the far boundary, that is

$$p_o(x=0,t) = p_o(x=L,t)\,. \quad (16)$$

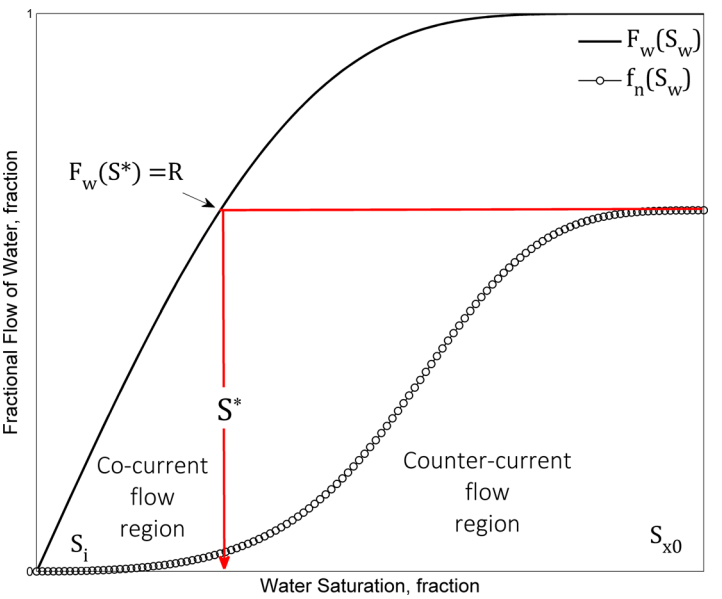

Figure 3. The solution of cocurrent displacements with some degree of countercurrent flow. The fractional flow function F_w is used to identify a critical water saturation, S^*, at which regions of co and countercurrent flow take place. The R value, used to compute the solution, explicitly specifies the amount of countercurrent flow in the system, since $R = q_t/q_{x0}$. Furthermore, between S^* and S_i, the nonwetting phase moves in the same direction with the wetting phase and the flow is unidirectional. Between S^* and S_{x0}, however, fluids move in opposite directions (counter-current), while at S^* only the wetting phase is flowing ($q_t = q_w$).

It is assumed in equation (16) that capillary back pressure, which is the difference in pressure between oil and water at the inlet boundary [*Haugen et al.*, 2014], is negligible. Nevertheless, this assumption is considered valid as long as S_{x0} is kept close to $(1 - S_{orw})$, for strongly water-wet media. The value of R can then be determined implicitly by satisfying the pressure boundary condition in equation (16). A mathematical expression for oil phase pressure, as a function of distance, is obtained from Darcy's equation by solving for $p_o(x,t)$

$$p_o(x,t)=p_o(0,t)-\frac{\mu_o}{k}\frac{A}{\sqrt{t}}\int_0^x\frac{R(t)-F_w(\beta,t)}{k_{ro}(\beta,t)}\mathrm{d}\beta\,. \tag{17}$$

The detailed mathematical derivation of equation (17) is provided in Appendix B. This expression can be used to compute the oil phase pressure as a function of distance and time. The functions $F_w(x,t)$ and $k_{ro}(x,t)$ depends implicitly on x and t through $S_w(x,t)$, which can be computed from equation (8). Therefore, the oil pressure can be determined at the far boundary by substituting $x=L$ in equation (17), subject to equation (16); this gives the following implicit relation for R:

$$\int_0^L\frac{R(t)-F_w(x,t)}{k_{ro}(x,t)}\mathrm{d}x=0\,. \tag{18}$$

The algorithm for such systems works by first selecting a value for R, such that $0<R<1$, then $F_w(S_w)$, $F'_w(S_w)$ and A are computed using equations (13), (14), and (15), respectively, and finally S_w versus x is determined from equation (8). Using the selected R value, the condition in equation (18) is checked. If it is not satisfied, iterations are performed on R until convergence. Figure 5 depicts a schematic of typical oil pressure profiles for counter and cocurrent flow. This concept demonstrates the impact of system length on the degree of cocurrent flow and how the original solution fails to capture this behavior.

Upon closer examination of equation (18), important information on how the value of R depends on the advancing saturation front can be revealed. This is demonstrated by rewriting equation (18), for a given time t^*, as

$$R(t^*)\left(\int_0^{x_f}\frac{\mathrm{d}x}{k_{ro}(x,t^*)}+\int_{x_f}^{L}\frac{\mathrm{d}x}{k_{ro}(x,t^*)}\right)=\int_0^{x_f}\frac{F_w(x,t^*)}{k_{ro}(x,t^*)}\mathrm{d}x+\int_{x_f}^{L}\frac{F_w(x,t^*)}{k_{ro}(x,t^*)}\mathrm{d}x\,, \tag{19}$$

since $S_w(x,t^*)$ in the uninvaded region, between x_f and L, is at initial conditions, S_i, the function $k_{ro}(x,t^*)$ becomes fixed at $(\bar{k}_{ro})$; this is usually equal to unity when S_i is at irreducible conditions, while $F_w(x,t^*)$ is zero. This reduces equation (19) to

$$R(t^*)\left(\int_0^{x_f}\frac{\mathrm{d}x}{k_{ro}(x,t^*)}+\frac{L-x_f}{\bar{k}_{ro}}\right)=\int_0^{x_f}\frac{F_w(x,t^*)}{k_{ro}(x,t^*)}\mathrm{d}x\,. \tag{20}$$

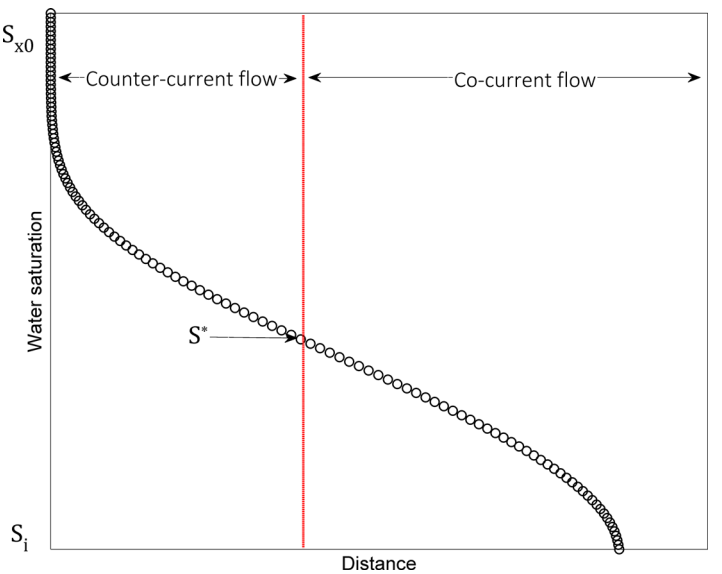

Figure 4. A schematic illustrating the solution of cocurrent with some degree of countercurrent flow. The critical saturation S^*, determined from the F_w plot, is used to identify regions of co and countercurrent flows in the porous media. Between S^* and S_i, the nonwetting phase moves in the same direction with the wetting phase and the flow is unidirectional. Between S^* and S_{x0}, however, fluids move in opposite directions (countercurrent), while at S^* only the wetting phase is flowing $(q_t=q_w)$.

It is readily seen from (20) that at $x_f=0$, we have $R=0$ indicting a complete countercurrent displacement; nevertheless, as x_f increases, R increases. Furthermore, when $x_f=L$, equation (20) reduces to

$$R(t^*)=\frac{\int_0^L\frac{F_w(x,t^*)}{k_{ro}(x,t^*)}\mathrm{d}x}{\int_0^L\frac{\mathrm{d}x}{k_{ro}(x,t^*)}}\,. \tag{21}$$

It can be easily seen that when the saturation front reaches the far boundary, the R value will always be less than unity and will never reach one, although it can be very close to one for large L. This is observed from the behavior of the functions inside the integrals in equation (21); as $x\to 0$, the functions

$1/k_{ro}(x,t^*) \to \infty$ and $F_w(x,t^*)/k_{ro}(x,t^*) \to \infty$. As $x \to L$, however, the function $1/k_{ro}(x,t^*)$ approaches the constant: $\left(1/\bar{k}_{ro}\right)$, while $F_w(x,t^*)/k_{ro}(x,t^*) \to 0$. The following inequality therefore holds:

$$\left(\int_0^L \frac{dx}{k_{ro}(x,t^*)}\right) > \left(\int_0^L \frac{F_w(x,t^*)}{k_{ro}(x,t^*)}dx\right). \tag{22}$$

This observation indicates that there will be a continuous production of the nonwetting fluid by countercurrent flow. The main reason behind this observation is the assumption of negligible capillary back pressure.

From equation (22), we also observe that the value of R for such systems is a function of time. The analytic solution, however, requires the value of R, and hence the imbibition rate function in equation (7), to be fixed throughout the displacement; from the start of the imbibition process until the time used to compute the solution. Consequently, the previous development ignores this time dependency of the R value. To rectify this issue and address the impact of having variable imbibition rate-functions, we use the principle of superposition. This is demonstrated next.

3.2. Superposition in Time

From the previous analysis, we show that R, which controls the imbibition rate parameter A, starts at zero at $t = 0$ and then increases in a monotone fashion until reaching a maximum value when the wetting front reaches the end of the system. The condition in equation (18) can be used to find a set of R values that describe the behavior of a particular physical system over time. These values represent the solutions to the constant imbibition rate functions, equation (7). Nevertheless, we postulate that they can be used to accurately model systems with variable imbibition rate functions using the principle of superposition. The key concept is to break down the complex problem into smaller parts, where the constant-R solution is considered valid. The total system behavior is then determined from the summation of the solutions of the individual parts. Although the original two-phase flow equation is highly nonlinear in fluid saturation, we will show that the superposition in time is applicable to model the distance profile under variable imbibition rate functions along a constant saturation path. We estimate the position of the front x_f for cocurrent flow at time t. This reduces the illustration to a single saturation point only (S_i). We also use a simple variable-R system that consists of two-step functions. It is assumed that the R values, and their corresponding A values, satisfy the specific condition of the physical system in hand. For $t \leq t_1$, the function $x_f(t)$ is determined directly from equation (8) with $R = R_0$ and $S_w = S_i$. It is observed that along a constant saturation path, both A and $F'_w(S_w)$ depend on, and stay constant for a particular R value.

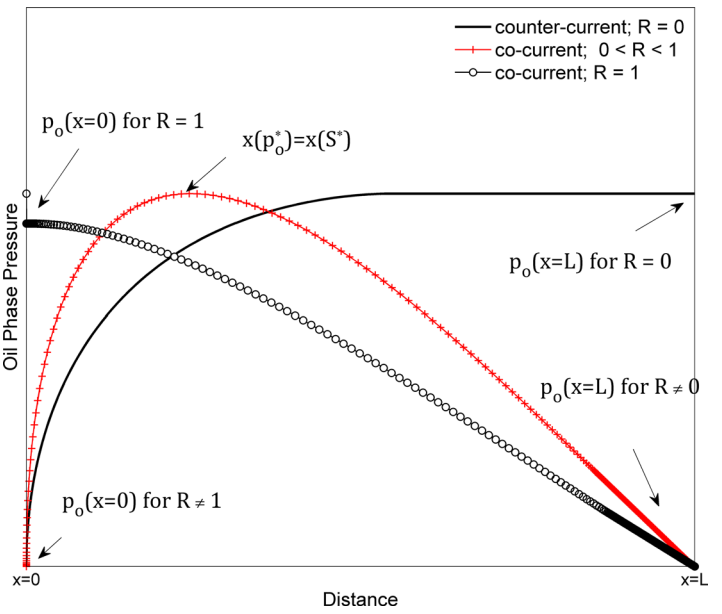

Figure 5. The behavior of the oil-phase pressure as a function of distance. For countercurrent flow, the oil pressure increases in a monotone fashion until reaching a plateau where is stays constant. The far boundary ($x = L$) for such systems is closed. The unidirectional cocurrent flow, on the other hand, shows a pressure gradient in the direction of flow throughout the system. For the cocurrent flow with some degree of countercurrent, the oil pressure takes a bell-shaped curve, where at the inflexion point q_o is zero and the oil moves into different directions from that point. The pressure drop for oil across the system is zero in this case.

To simplify the notation, we defined a new function $Y(R)$ as follows:

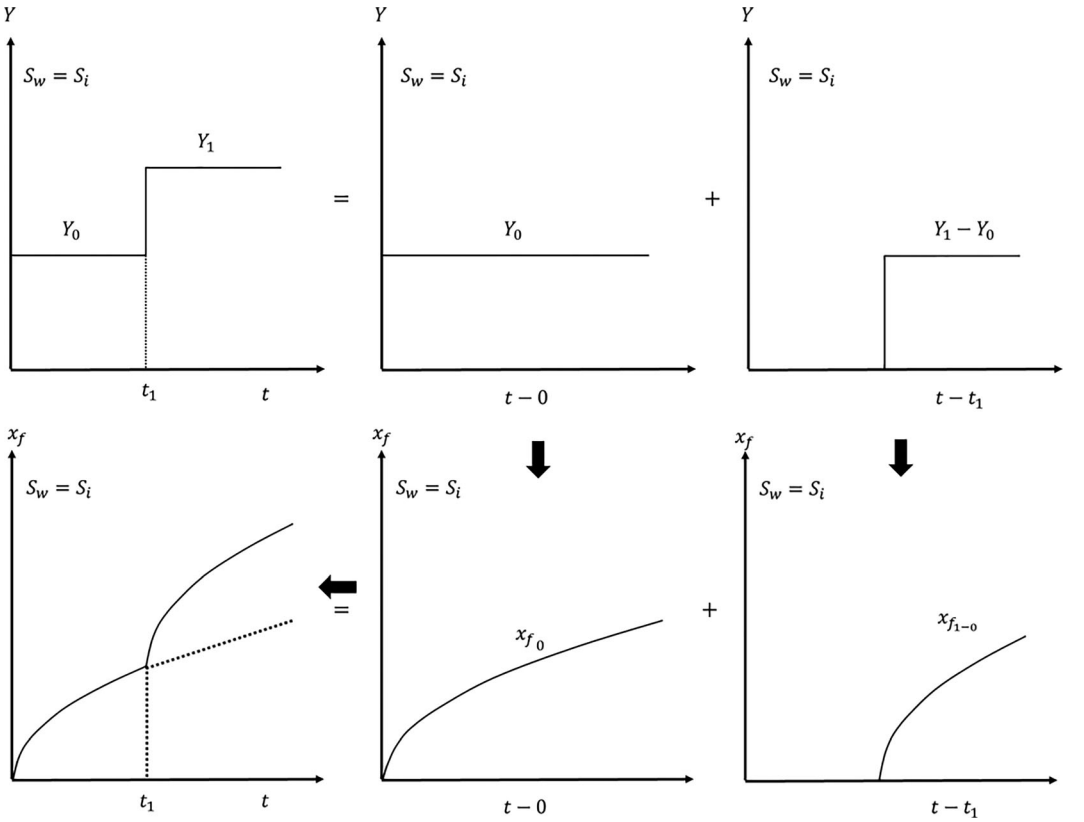

Figure 6. A schematic describing the principle of superposition in time to estimate the position of the front at a constant saturation path. The system considered a simple case of two-step functions. The solution is obtained by breaking down the problem into two simpler problems where the analytic solution can be applied. The final answer is then attained by combining the two simple answers. The main justification for using the principle of superposition is that along a fixed saturation point, superposition is imposed in the distance.

$$Y(R) = \frac{2A(R)}{\phi}\frac{\mathrm{d}F_w(R)}{\mathrm{d}S_w}\Big|_{S_w=S_i}; \tag{23}$$

therefore for $t \leq t_1$, the distance of the front is calculated as

$$x_f(t) = Y(R_0)\sqrt{t}\,. \tag{24}$$

For $t > t_1$, however, equation (24) is no longer valid and the solution can be obtained by splitting the system into two simpler parts. This is demonstrated graphically in Figure 6. The impact of the incremental increase $(Y_1 - Y_0)$ is seen only when $t > t_1$ and its influence on the position of the front is obtained by adding its solution to the case when Y_0 continues until $t > t_1$;

$$x_f(t) = Y(R_0)\sqrt{t} + (Y(R_1) - Y(R_0))\sqrt{t - t_1}\,, \tag{25}$$

where $R_0 = 0$. This analogy can be extended to an arbitrary number of steps and for different saturation paths as well. The final solution is then given by the convolution sum in the form

$$x(t, S_w) = Y(R_0)\sqrt{t} + \sum_{i=1}^{n}(Y(R_i, S_w) - Y(R_{i-1}, S_w))\sqrt{t - t_i}\,. \tag{26}$$

Equation (26) can also be converted into a convolution integral in the limit as $(t - t_i)$ goes to zero. This achieved by multiplying and dividing equation (26) by $\Delta\tau_i = t - t_i$;

$$x(t, S_w) = Y(R_0)\sqrt{t} + \int_0^t \frac{\mathrm{d}Y(R_\tau, S_w)}{\mathrm{d}\tau}\sqrt{t - \tau}\;\mathrm{d}\tau\,. \tag{27}$$

Upon integrating equation (27) by parts:

$$x(t,S_w)=\frac{1}{2}\int_0^t \frac{Y(R_\tau,S_w)}{\sqrt{t-\tau}}\mathrm{d}\tau\,. \tag{28}$$

This gives the final expression for computing the distance profile under variable imbibition rate functions. The solution is now attainable by first calculating the relationship between R and time. This is accomplished by dividing the interval into several regions where $Y(R,S_w)$ is computed for each region individually. As more regions are added, accurate results are obtained. The final answer is then determined from the convolution sum in equation (26). This will be further investigated in an illustrative example below.

4. Approximate Solutions to Co and Countercurrent Flow

The original analytical solution for equation (9) can either be solved using the implicit integral [*McWhorter and Sunada*, 1990] or the pseudospectral approach [*Bjørnarå and Mathias*, 2013]. Both methods may require advanced programming skills and careful numerical implementation. In this section, we present an approximate analytical solution that requires fewer iterations and is much simpler to implement. For this purpose, we use a perturbative approach [*Bender et al*., 1989] to solve the nonlinear second-order ordinary differential equation (9). The key idea is to introduce a parameter δ into the nonlinear equation such that it can be converted into an infinite sequence of linear ordinarily differential equations that can be easily solved to arbitrary accuracy. Rewriting equation (9) in the following form

$$\left(F_w^{\delta}-f_n\right)F''_w=-\omega D\,, \tag{29}$$

with some arbitrary exponent δ. In equation (29), ω is a constant whose value is given by

$$\omega=\frac{\phi}{2A^2(1-f_iR)^2}\,. \tag{30}$$

For $\delta=0$, equation (29) reduces into a linear ordinary differential equation that can be solved explicitly, while the original nonlinear equation is recovered for $\delta=1$. Now, the function F_w depends on δ. We further assume that it has a formal power series expansion in δ, and the general solution for F_w is then given by:

$$F_w(S_w,\delta)=F_0(S_w)+\delta F_1(S_w)+\delta^2F_2(S_w)+\ldots\,. \tag{31}$$

We now substitute equation (31) into (29) and expand in terms of δ;

$$\begin{aligned} &F''_0(1-f_n)\,\delta^0\\ &+\left(F''_0\ln F_0+F''_1(1-f_n)\right)\delta^1\\ &+\left(F''_0\left(\frac{1}{2}\ln^2F_0+\frac{F_1}{F_0}\right)+F''_2(1-f_n)+F''_1\ln F_0\right)\delta^2\\ &+\ldots=-\omega D\,. \end{aligned} \tag{32}$$

By comparing powers of δ in equation (32), we obtain a sequence of linear equations, along with their associated boundary conditions. For the first three terms, we obtain

$$F''_0=\frac{-\omega D}{(1-f_n)}\,,\qquad F_0(S_i)=0,\ F_0(S_{x0})=1\,, \tag{33}$$

$$F''_1=\frac{\omega D}{(1-f_n)^2}\ln F_0\,,\qquad F_1(S_i)=F_1(S_{x0})=0\,, \tag{34}$$

$$F''_2=\frac{\omega D}{(1-f_n)^2}\left(\frac{-(1+f_n)}{2(1-f_n)}\ln^2F_0+\frac{F_1}{F_0}\right),\qquad F_2(S_i)=F_2(S_{x0})=0\,. \tag{35}$$

4.1. Zeroth-Order Calculation

The solution for equation (33) subject to the specified boundary conditions is given by (the detailed derivation is in Appendix C)

$$F_0(S_w)=S_n(S_w)-\omega(T_0(S_w)-T_0(S_i)(1-S_n(S_w)))\,, \tag{36}$$

where S_n is the normalized water saturation, given by

$$S_n(S_w)=\frac{S_w-S_i}{S_{x0}-S_i}\,. \tag{37}$$

The integral functions $T_0(S_w)$ and $T_0(S_i)$ are computed as

$$T_0(S_w)=\left(\int_{S_w}^{S_{x0}}\frac{(\beta-S_w)D(\beta)}{1-f_n(\beta)}\mathrm{d}\beta\right)\,, \tag{38}$$

$$T_0(S_i)=\left(\int_{S_i}^{S_{x0}}\frac{(\beta-S_i)D(\beta)}{1-f_n(\beta)}\mathrm{d}\beta\right)\,. \tag{39}$$

4.2. First-Order Calculation

Similar to the previous step, the solution for equation (34) is given by

$$F_1(S_w)=\omega(T_1(S_w)-T_1(S_i)(1-S_n(S_w)))\,, \tag{40}$$

with

$$T_1(S_w)=\left(\int_{S_w}^{S_{x0}}\frac{(\beta-S_w)D(\beta)}{(1-f_n(\beta))^2}\ln F_0(\beta)\,\mathrm{d}\beta\right)\,, \tag{41}$$

$$T_1(S_i)=\left(\int_{S_i}^{S_{x0}}\frac{(\beta-S_i)D(\beta)}{(1-f_n(\beta))^2}\ln F_0(\beta)\,\mathrm{d}\beta\right)\,. \tag{42}$$

4.3. Second-Order Calculation

Similar to the previous steps, the solution for equation (35) is given by

$$F_2(S_w)=\omega(T_2(S_w)-T_2(S_i)(1-S_n(S_w)))\,, \tag{43}$$

with

$$T_2(S_w)=\left(\int_{S_w}^{S_{x0}}\frac{(\beta-S_w)D(\beta)}{(1-f_n(\beta))^2}\left(\frac{-(1+f_n(\beta))}{2(1-f_n(\beta))}\ln^2 F_0(\beta)+\frac{F_1(\beta)}{F_0(\beta)}\right)\mathrm{d}\beta\right)\,, \tag{44}$$

$$T_2(S_i)=\left(\int_{S_i}^{S_{x0}}\frac{(\beta-S_i)D(\beta)}{(1-f_n(\beta))^2}\left(\frac{-(1+f_n(\beta))}{2(1-f_n(\beta))}\ln^2 F_0(\beta)+\frac{F_1(\beta)}{F_0(\beta)}\right)\mathrm{d}\beta\right)\,. \tag{45}$$

4.4. *n*th-Order Calculation

It is observed from $F_{1,2}(S_w)$ that higher-order equations will have the following form:

$$F_n(S_w)=\omega(T_n(S_w)-T_n(S_i)(1-S_n(S_w)))\,, \tag{46}$$

where the integrals $T_n(S_w)$ is determined by comparing powers of δ in equation (32). We have determined the first three coefficients of the series. Nevertheless, more terms can be added as needed depending on the desired accuracy.

4.5. Calculation of ω

Although the integrals in equations (41) and (44) do not look simple to evaluate, their computations are explicit and involve straightforward mathematics. Their calculations are far more rapid than the implicit

integral solutions. The final approximate solution is found by summing up the series in equation (31) for $\delta = 1$. However, the parameter ω is unknown since it contains the parameter A, which controls the imbibition rate. To determine ω, we use, following *McWhorter and Sunada* [1990], the condition that $F\prime(S_{x0})$ must be zero to prevent the movement of S_{x0} at $x = 0$ into the porous medium. This condition gives the following implicit relationship for ω:

$$\omega = \left(T_0(S_i) - \sum_{i=1}^{n} T_n(S_i)\right)^{-1}. \tag{47}$$

Since $T_n(S_i)$ for $n > 0$ depends on ω, iterations are required to determine its value. Nevertheless, a very good estimation of ω is achieved from $T_0(S_i)$ and hence can be used as a convenient first guess. The final solution, after substituting the individual solutions in equations (36), (40), and (43) into equation (31) with $\delta = 1$, is given by

$$F_w(S_w) = 1 - \omega\left(T_0(S_w) - \sum_{i=1}^{n} T_n(S_w)\right), \tag{48}$$

$$F\prime_w(S_w) = \omega\left(G_0(S_w) - \sum_{i=1}^{n} G_n(S_w)\right), \tag{49}$$

where the integral functions $G_n(S_w)$ for $n \geq 0$ are found exactly as $T_n(S_w)$ in (38), (41), and (44), but without the term $(\beta - S_w)$ that appears at the beginning of each integral;

$$G_0(S_w) = \left(\int_{S_w}^{S_{x0}} \frac{D(\beta)}{1 - f_n(\beta)}\, \mathrm{d}\beta\right), \tag{50}$$

$$G_1(S_w) = \left(\int_{S_w}^{S_{x0}} \frac{D(\beta)}{(1 - f_n(\beta))^2} \ln F_0(\beta)\, \mathrm{d}\beta\right), \tag{51}$$

and

$$G_2(S_w) = \left(\int_{S_w}^{S_{x0}} \frac{D(\beta)}{(1 - f_n(\beta))^2}\left(\frac{-(1 + f_n(\beta))}{2(1 - f_n(\beta))} \ln^2 F_0(\beta) + \frac{F_1(\beta)}{F_0(\beta)}\right) \mathrm{d}\beta\right). \tag{52}$$

The calculations proceed conveniently by first calculating $T_0(S_i)$ from which ω is first approximated and used for the subsequent calculations for $T_n(S_w)$ and $F_n(S_w)$ for $n \geq 0$. The value of ω is then updated and the calculations are repeated until convergence.

In this study, we will be using the first three terms of the series in equations (48) and (49) to approximate the solution. It is not known at this stage if the series will converge or diverge. Nevertheless, even if it diverges, there are many techniques, such as the Pade` approximation technique [*Bender and Orszag*, 1999] that can be used to sum up a divergent series and obtain a meaningful answer. In the next section, the performance of the approximate solution will be evaluated and compared with the exact integral solutions.

5. Illustrative Example

We now present a case study in which numerical, analytical, and approximate solutions are applied and compared using synthetic data. Fluid and petrophysical rock properties are summarized in Table 1. Capillary pressure and relative permeability curves (Figure 7) are generated using a power law model.

In this case study, error norms and convergence rates between analytical and numerical solutions will be calculated for countercurrent, and cocurrent displacements with some degree of countercurrent flow.

Table 1. Fluid and Petrophysical Rock Properties

Rock Properties	L	0.3048 m
	W	0.1524 m
	H	0.1524 m
	k	9.8692×10^{-15} m^2
	ϕ	0.25
Fluid properties	μ_w	1.00×10^{-3} Pa.s
	μ_o	1.00×10^{-3} Pa.s
Petrophysical properties:	S_{wir}	0.15
	S_{orw}	0.25
	$\bar{k}_{rw}$	0.25
	$\bar{k}_{ro}$	0.95
	n_w	2
	n_o	3
	$\bar{p}_c$	6.895×10^4 Pa
	n_c	3

5.1. Comparison Between Analytical and Numerical Solutions for Countercurrent Displacement

We start first by comparing analytical with numerical solutions for countercurrent flow. The analytical solution is determined as outlined earlier; the fractional flow $F_w(S_w)$ in equation (13) is computed with $R=0$. After that, the functions $FI_w(S_w)$ and A are computed conveniently using equations (14) and (15) and plugged into equation (8) to determine the distance. The numerical simulation, on the other hand, is found using a conventional finite-difference formulations with IMPES flow solver as described in detail in Appendix A using a 500 grid-cell model that is initially saturated with movable oil and immobile water. Countercurrent flow is imposed by setting the water saturation to a maximum value $(1-S_{orw})$ at the inlet boundary ($x=0$) with arbitrary oil phase pressure (p_o is set to zero in this test case for convenience). At the far boundary ($x=L$), a no-flow ($Q_o=0$) boundary condition is imposed. The comparison between the two methods is demonstrated graphically in Figure 8 using the invariant saturation profiles (S_w versus $x/\sqrt{t}$) at different oil-to-water viscosity ratios (μ_o changes while μ_w is fixed to the value in Table 1). The plot indicates a very close match with slight deviations for very low oil-to-water viscosity ratios.

5.2. Cocurrent Displacement With Some Degree of Countercurrent Flow

The calculation of the cocurrent flow is performed for two times: early time $t_1=7,646$ s, and late time $t_2=98,888$ s. We first extract the pressure and saturation profiles at those specific times from the numerical simulation. Note that the implementation of the numerical solutions is similar to the countercurrent case, except that the fluids are now allowed to exit from the far boundary according to the condition in equation (16). Before computing the analytical solutions, we know that the saturation profile should be located somewhere between the countercurrent ($R=0$) and cocurrent case with no backflow ($R=1$). We also determine the fixed-R solutions, for demonstration purposes, at t_1 and t_2. The R values that satisfy the condition in equation (18) are found by iteration to be 0.647 and 0.921 for t_1 and t_2, respectively. The corresponding saturation profiles are shown in Figure 9. From the previous analysis of cocurrent flow with backflow, equations (19) and (20), the fixed-R solution is not valid since it assumes a constant value over the entire time duration, while R changes over time starting from $R=0$ at $t=0$. In this case, the saturation profile calculated using the fixed-R solution moves deeper into the rock away from the true position, but it also gives an upper limit to it. From this analysis, it is demonstrated that the true solution for t_1 is somewhere in between $R=0$ and 0.647, and for t_2, it is between $R=0$ and 0.921. Figure 9 indicates also how $x/\sqrt{t}$ scaling does not work for such systems.

We proceed with the fixed-R analytical solutions and compare them with the numerical solutions. The main purpose is to establish the physical significance of the analytical solutions using the fixed-R approach and how far it is from the numerical solutions before implementing the multiple-R method, which involves using convolution sums. For this, we compare the saturation profiles between the fixed-R and numerical solutions t_1 and t_2 (Figure 10). It is remarkable to see the close correspondence between the two solutions even without using the convolution sums. Moreover, the overestimation in t_2 is expected since the fixed-R is used over the entire time region. We compute the profiles of oil-phase pressure analytically using equation (17) and compare them with the numerical solutions. This is shown in Figure 11a. The trends are accurately captured; however, the numerical solutions slightly overestimate the oil phase pressure with maximum deviations near the inflection point. Nevertheless, Figure 11a shows how oil pressure profile has a humped shape curve as a function of distance. The magnitude of the pressure generally decreases indicating lower total production rates. In addition, the inflection points on the curves indicate the regions in which countercurrent and cocurrent flow take place. The

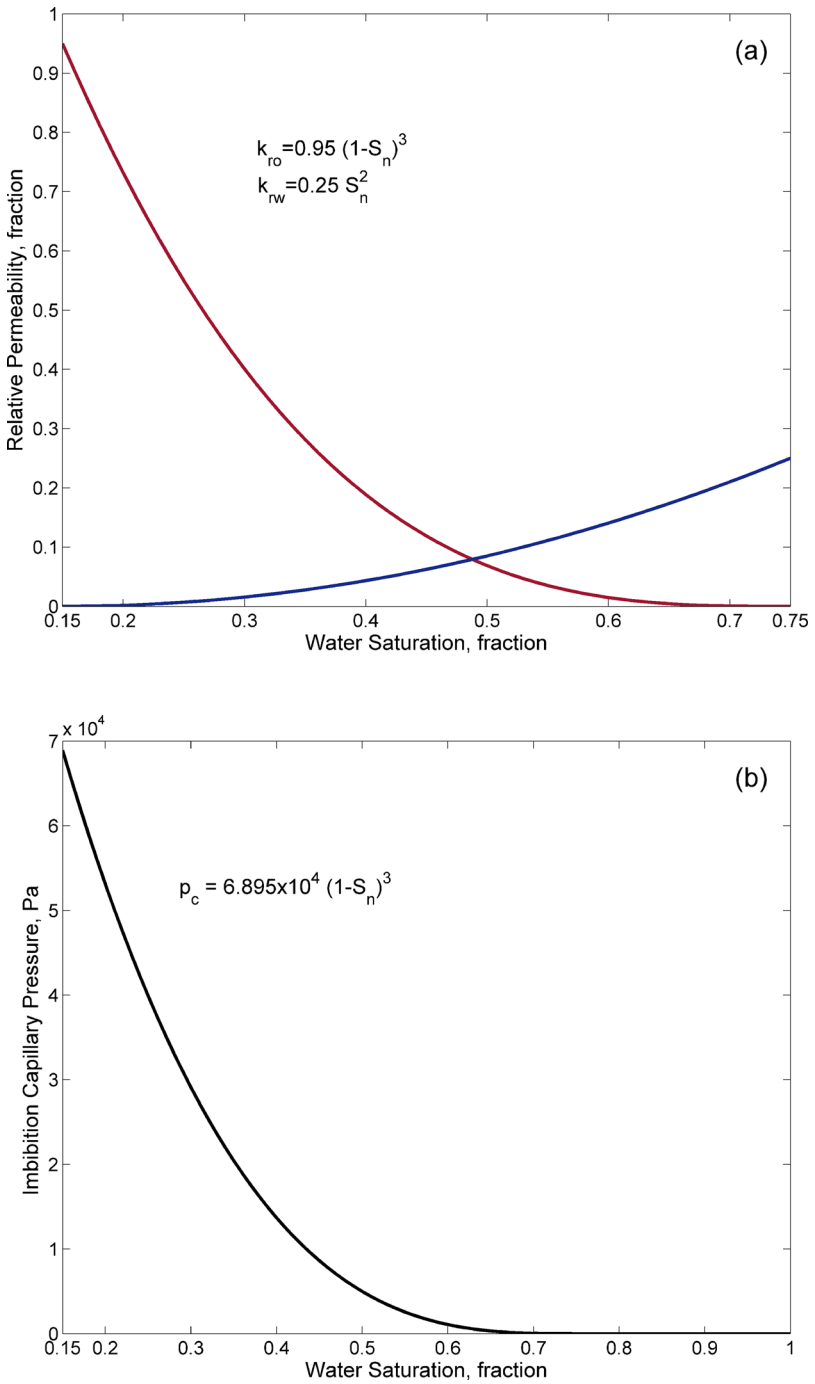

Figure 7. (a) Relative permeability and (b) capillary pressure curves for imbibition in strongly water-wet media used in the case study. The curves are generated using power law models using parameters in Table 1.

corresponding points on the distance axis ($x_1^* \approx 0.047, x_2^* \approx 0.071$) are identified and used to find the critical saturation points on the saturation profiles ($S_1^* \approx 0.31, S_2^* \approx 0.47$). In Figure 11b a simpler method to extract S_1^* and S_2^* directly from the fractional flow function is by reading the saturation point that corresponds to the point R on the fractional flow curve. This is explained graphically in Figure 12. The computed F_w curves for R_1 and R_2 are plotted against water saturation. Unlike countercurrent displacement (F_w at $R = 0$), the fractional flow for cocurrent flow changes over time depending on the value of R. The critical saturations obtained from the fractional flow curves in Figure 12 exactly match the values

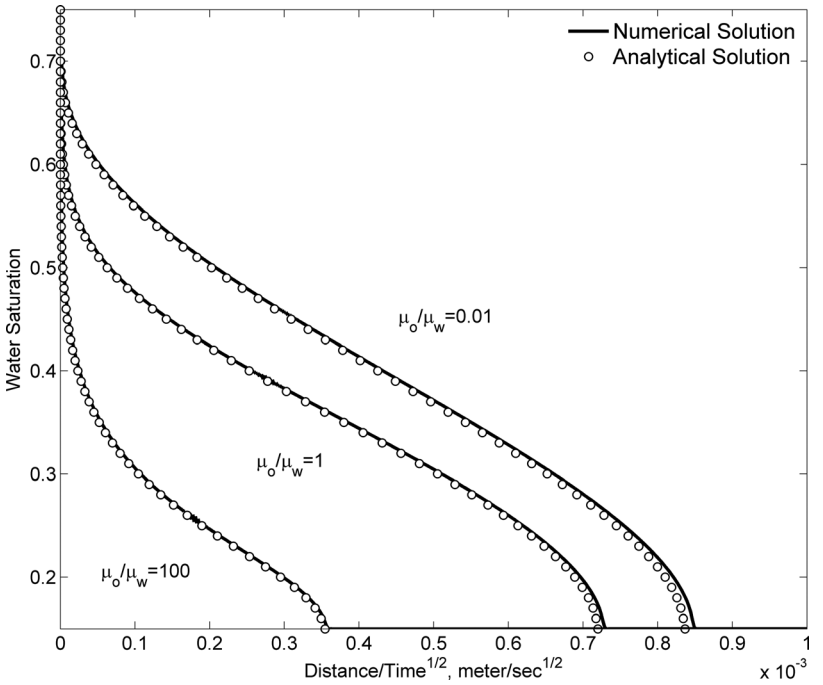

Figure 8. Comparison between analytical and numerical solutions for countercurrent flow at different viscosity ratios. Numerical simulations are found using 500 grid-cells in the flow direction.

observed from the pressure and saturation profiles in Figure 11. This example illustrates the physical significance of the R value and its role in controlling the amount of countercurrent flow in cocurrent displacements.

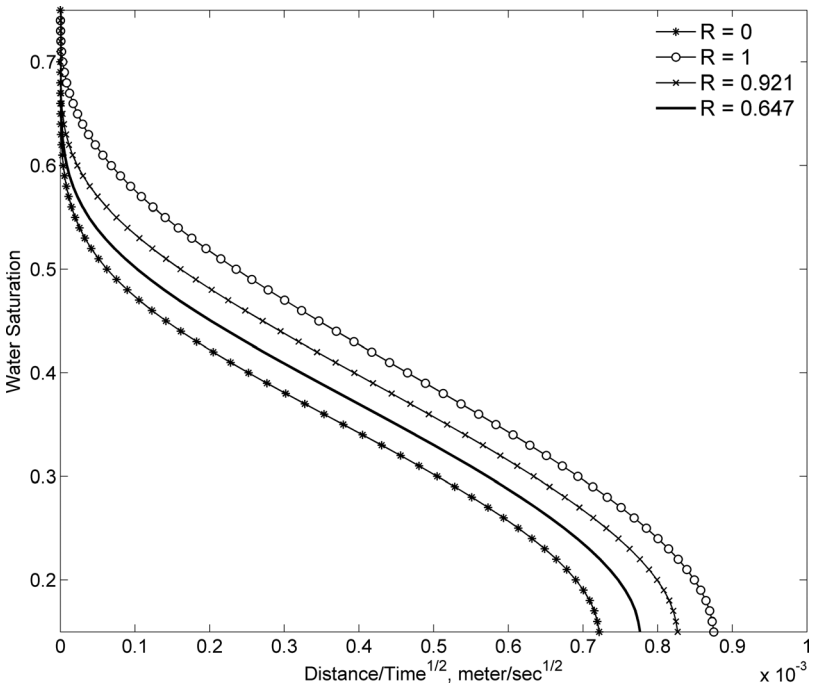

Figure 9. Saturation profiles versus $x/\sqrt{t}$ for different R values. The solutions are valid for fixed-R values. For cocurrent flow with some degree of cocurrent displacement, the solution is always bounded between $R = 0$ and a maximum value that satisfies the system condition at a specific time. The fixed-R solution ignores the history of the imbibition rate, assuming that a constant (the current) ratio of co to countercurrent imbibition is used during the entire displacement process.

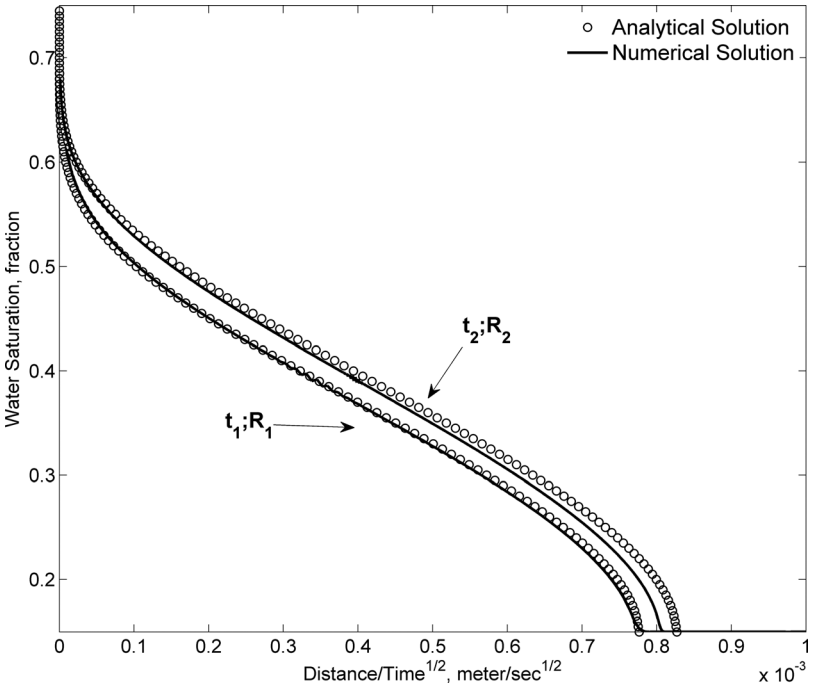

Figure 10. Comparison between the fixed-*R* and numerical solutions for cocurrent flow. Note the difference in the saturation profiles at t_1 and t_2 which do not follow an $x/\sqrt{t}$ scaling. The analytical solution using the fixed-*R* approximation is expected to overestimate the true saturation profiles since *R* changes with time. Nevertheless, the fixed-*R* solution shows very close correspondence to the numerical solution and hence may be used as a good approximation to the solution, especially for early times. The numerical simulations are performed using 500 grid-cells.

We now attempt to compute more accurate saturation profiles using the convolution sums in equation (26). We do this for t_2 at which the largest deviation from the true solution is expected to be. The solution is obtained by dividing the time interval into equal subintervals. The number of steps is used to determine the number of intervals used in the calculations. In the formulation used in equation (26), the number of equal time intervals corresponds to $n+1$. The duration for each subinterval is, therefore, $t/(n+1)$. It is not mandatory to have equal time intervals for the solution to be valid although this is what we do here for illustrative purposes. Once the time intervals are decided, the corresponding *R* values are determined for each discrete time using the fixed-*R* method described earlier. The convolution sum, in equation (26), is then used to obtain the final solution. Following this procedure, a sensitivity study is done to investigate the impact of *n* on the calculated saturation profiles. This is shown in Figure 13. The comparison indicates rapid convergence with *n*. In fact, even the fixed-*R* solution, whose solution requires no convolution sums at all, is considered a good approximation to the true solution.

It is observed from Figure 13 that the maximum error occurs at the saturation front. The true position of the front can be estimated by extrapolating the curve of $x_f(n)$ versus $1/n$ to 0. This is shown graphically in Figure 14. The data fit nicely into a linear curve. As $n \to \infty$, $1/n \to 0$ and the true position of the front is estimated to be near 0.2564. Using this value as a reference, the maximum error is calculated as a function of *n*. This is demonstrated graphically in Figure 15. It is remarkable to see in this example that the maximum absolute error in the fixed-R solution is less than 1.5%. This indeed makes a very good practical approximation to the true solution, without the need to use the convolution sums. If they are used, the error decreases significantly as more steps are added. However, even for a few number of steps, the maximum error is shown to be less than 1% for $n = 5$.

We now look into how the *R* values change over time. Figure 16 shows the plot for the $n = 100$ case. As mentioned earlier that the *R* values satisfy the system boundary conditions in equation (18), but for the fixed-*R* solution. The final saturation profile, computed using the convolution sums, however, might not satisfy equation (18). For such cases, the *R* values in Figure 16 are updated using the final saturation profiles, and the calculations are repeated until convergence is reached.

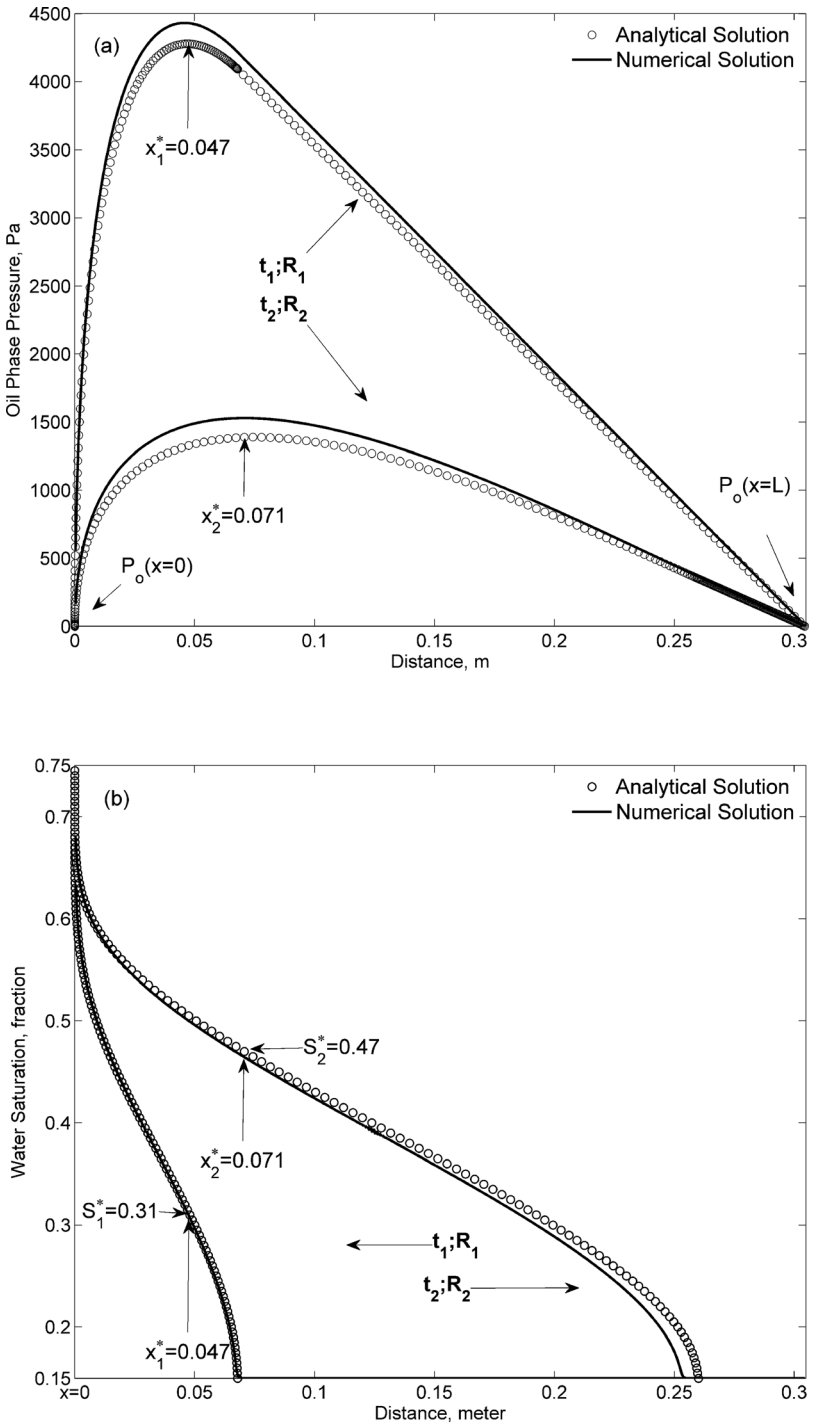

Figure 11. Comparison of (a) oil pressure and (b) water saturation profiles between the fixed-*R* approximation and numerical solutions for cocurrent flow. The critical saturations increases as the saturation front moves into the porous medium, indicating more cocurrent, and less countercurrent flow, with time.

It is found that the data can be modeled accurately with the following mathematical expression:

$$R(t)=\sum_{n=1}^{4} a_n t^{\frac{1}{n}}, \tag{53}$$

where a_n are fitting coefficients. Their values are: $a_1=7.149\times10^{-6}$, $a_2=-0.021$, $a_3=0.2495$, and $a_4=-0.2661$. The behavior of R with time indicates how the inverse proportionality of the imbibition rate

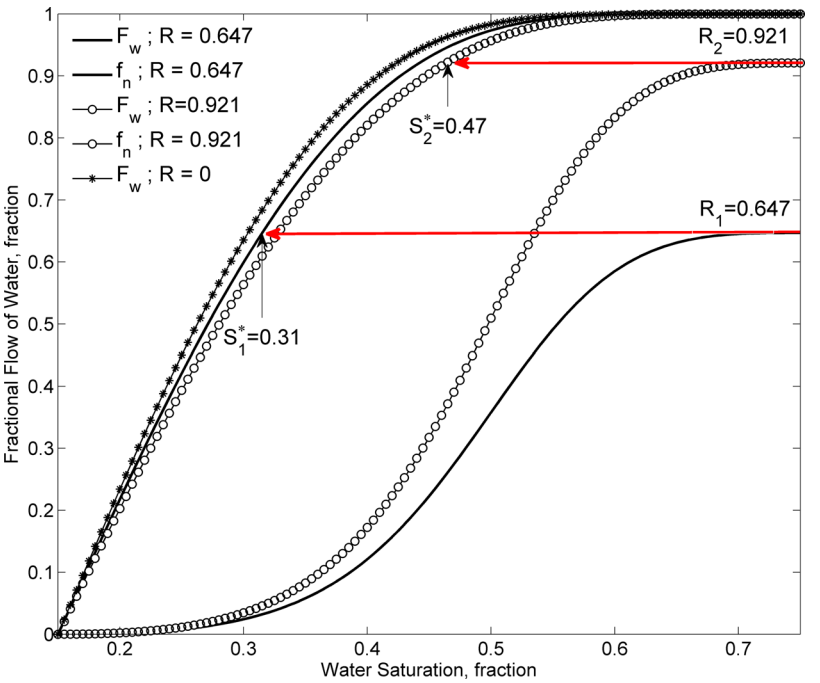

Figure 12. The fractional flow functions F_w for counter and cocurrent flow at different R values and the identification of the critical saturation points used to locate counter and cocurrent flow regions. It is observed that F_w changes slightly with R.

to $\sqrt{t}$ has disappeared. Indeed, the impact of the system length on the imbibition rate for cocurrent flow is of great importance. The amount of cocurrent flow increases sharply at early times before it steadily rises as it reaches the far boundary, while the amount of countercurrent flow decreases significantly and stays at a very low magnitude. However, the flow due to countercurrent flow never ceases due to the assumption of

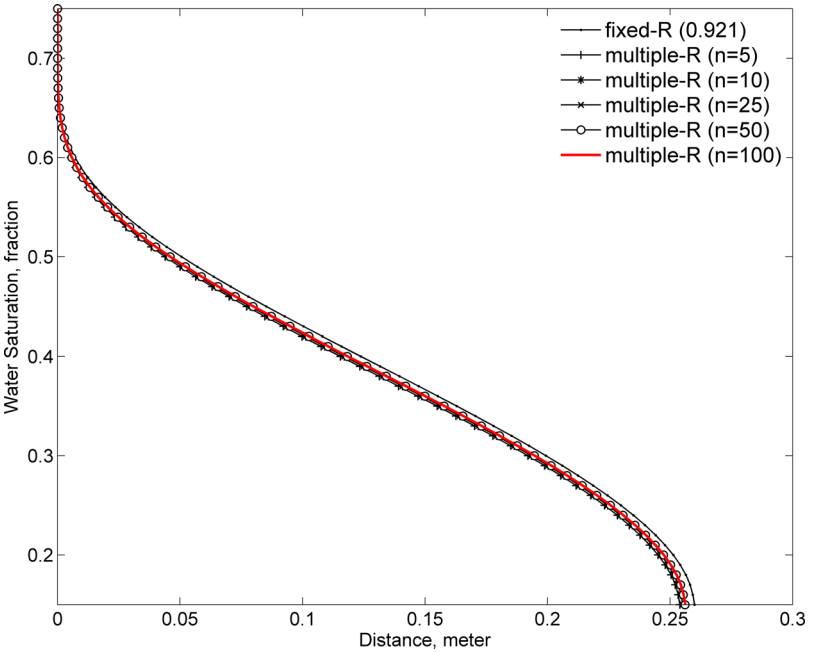

Figure 13. Water saturation profiles computed using the convolution sums for different steps. The number of equal time subintervals used in the convolution sums is $n + 1$. As n increases, the solution is more accurate. The comparison indicates close match even for the fixed-R solution, representing good approximation to the analytical solutions.

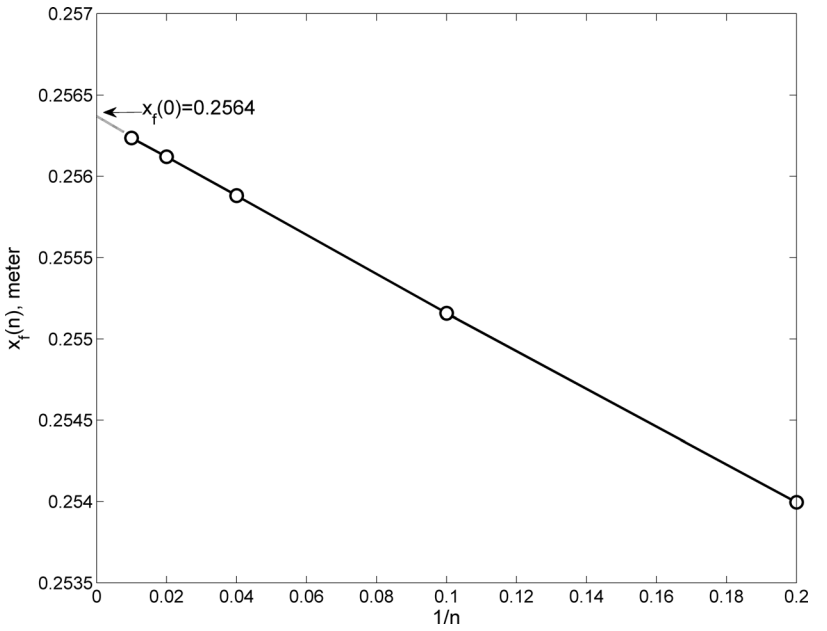

Figure 14. The position of the front (x_f) as a function of the reciprocal of the number of steps in the convolution sums (n). The estimation of the true front position is made as $n \rightarrow \infty$, which is $x_f \approx 0.2564$.

negligible capillary back pressure. Nevertheless, this assumption can be relaxed by modifying equation (18). This could be investigated in future studies.

We next compare the saturation profiles between the numerical and analytical solutions for cocurrent flow. For the analytical solution, we use the multiple-R approach with 100 steps in the convolution sums. This is depicted in Figure 17. The results indicate a close match between the two quantities, with slight deviations near the front.

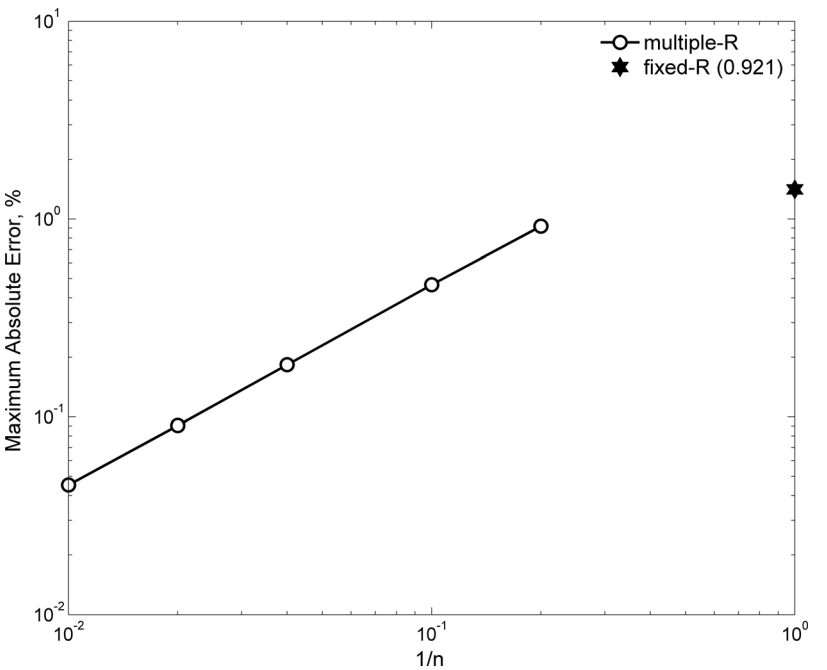

Figure 15. Absolute error in the calculated x_f as a function of the reciprocal of the number of steps in the convolution sums (n). The fixed-R solution is shown for comparison purposes only at $n = 1$. The error at the front represents the maximum error in the saturation profiles. The true x_f is used as the reference for calculating the errors.

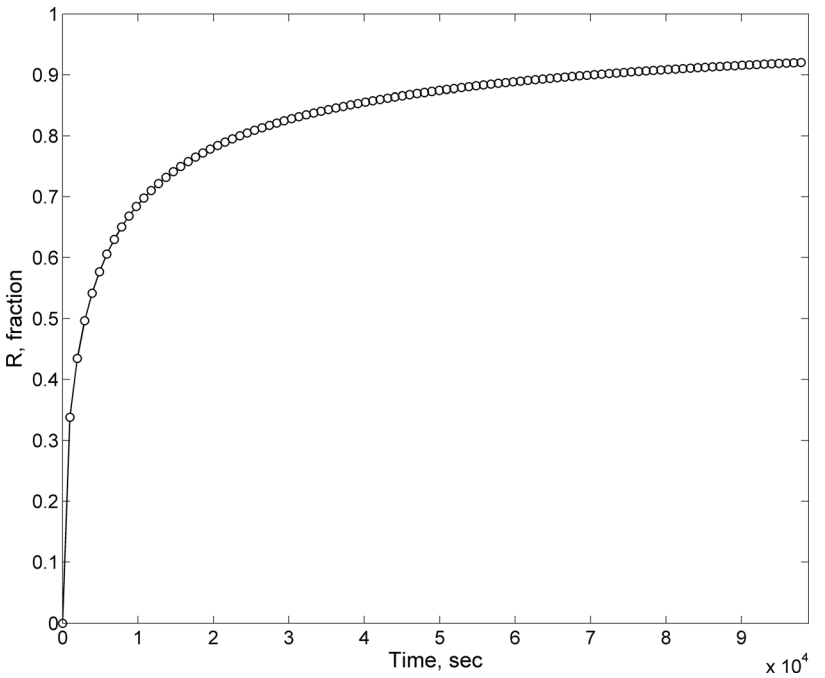

Figure 16. The behavior of the *R* parameter with time for cocurrent flow. The plot is generated using 100 data points. The curve is fitted precisely using equation (53).

5.3. Error Norms and Convergence Rates

In this section, a comprehensive convergence analysis between the numerical and analytical solutions is conducted for countercurrent flow. Error norms L_j for $j = 1, 2$ are calculated using the following expression:

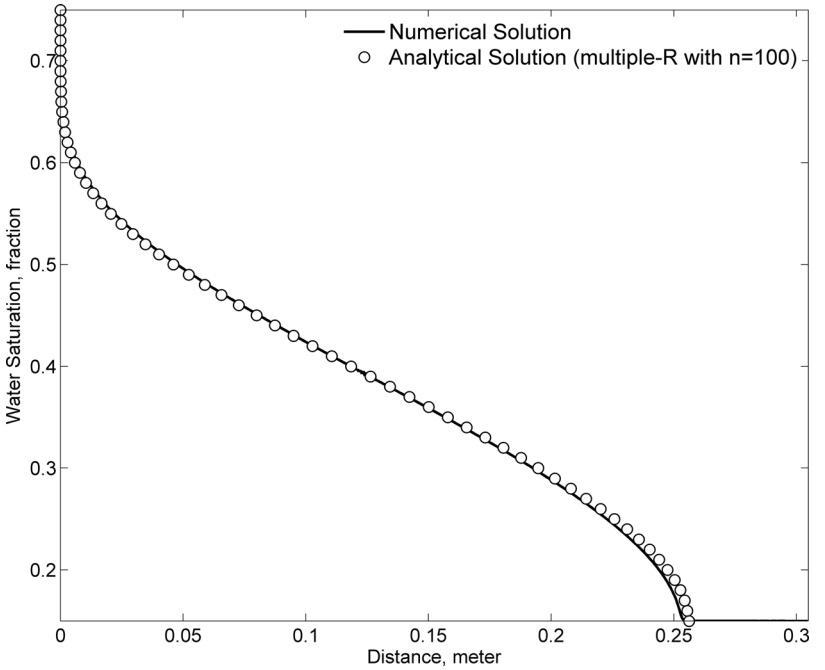

Figure 17. Comparison between numerical and analytical solutions for cocurrent flow with some degree of countercurrent. The analytical solution is generated using the convolution sum approach with $n = 100$.

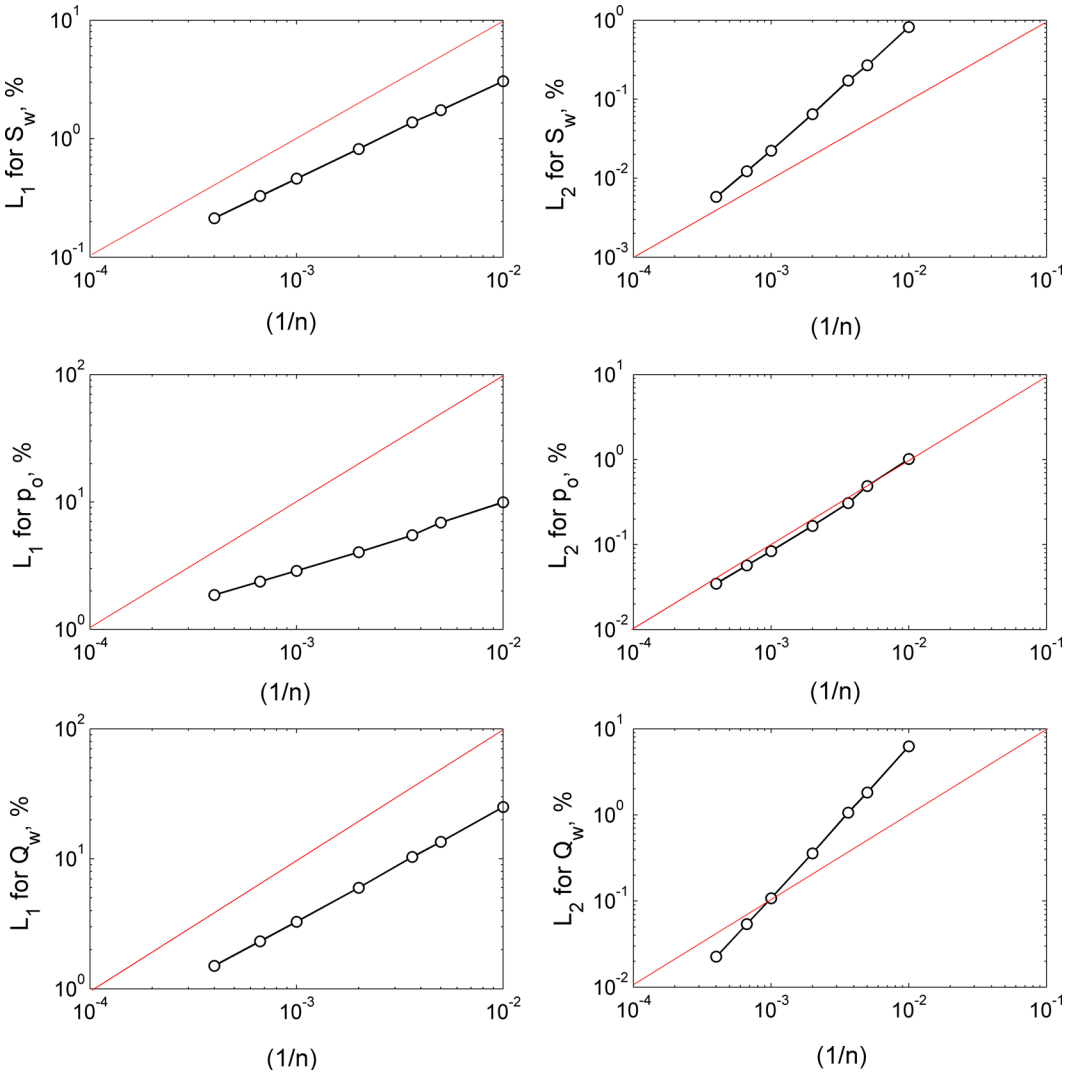

Figure 18. Error norms for p_o, S_w, and Q_w as function of the reciprocal of the number of grid cells $(1/n)$. The order of convergence of pressure is approximately half that for saturation and flux. It is possible that flux and the evolution of saturation are related to a pressure gradient and not the absolute value itself and therefore in a numerical implementation the pressure may converge slowly, even if the flow rates are captured accurately.

$$L_j = \left(\frac{\sum_{i=1}^{n} |x_i^{analytical} - x_i^{numerical}|^j}{\sum_{i=1}^{n} |x_i^{analytical}|^j} \right)^{\frac{1}{j}}, \tag{54}$$

where n here is the number of grid-cells in the numerical model and $i = 1, 2, \ldots, n$. The x variable takes the following parameters $\{p_o; S_w; Q_w\}$. Analytical calculations for S_w and Q_w are found using the implicit integral solutions presented in equations (13), (14), and (15), while equation (17) is used to find $p_o(x)$.

Figure 18 depicts the relationship between the error norms, represented by L_j, for p_o,S_w, and Q_w and the reciprocal of the number of grid cells $(1/n)$. The analysis indicates a slow convergence of order one for S_w and Q_w while a slower convergence rate is observed for pressure. The order of convergence of pressure is approximately half that for saturation and flux. A possible reason is that flux and the evolution of saturation are related to a pressure gradient and not the absolute value itself and therefore in a numerical implementation the pressure may converge slowly, even if the flow rates are captured accurately.

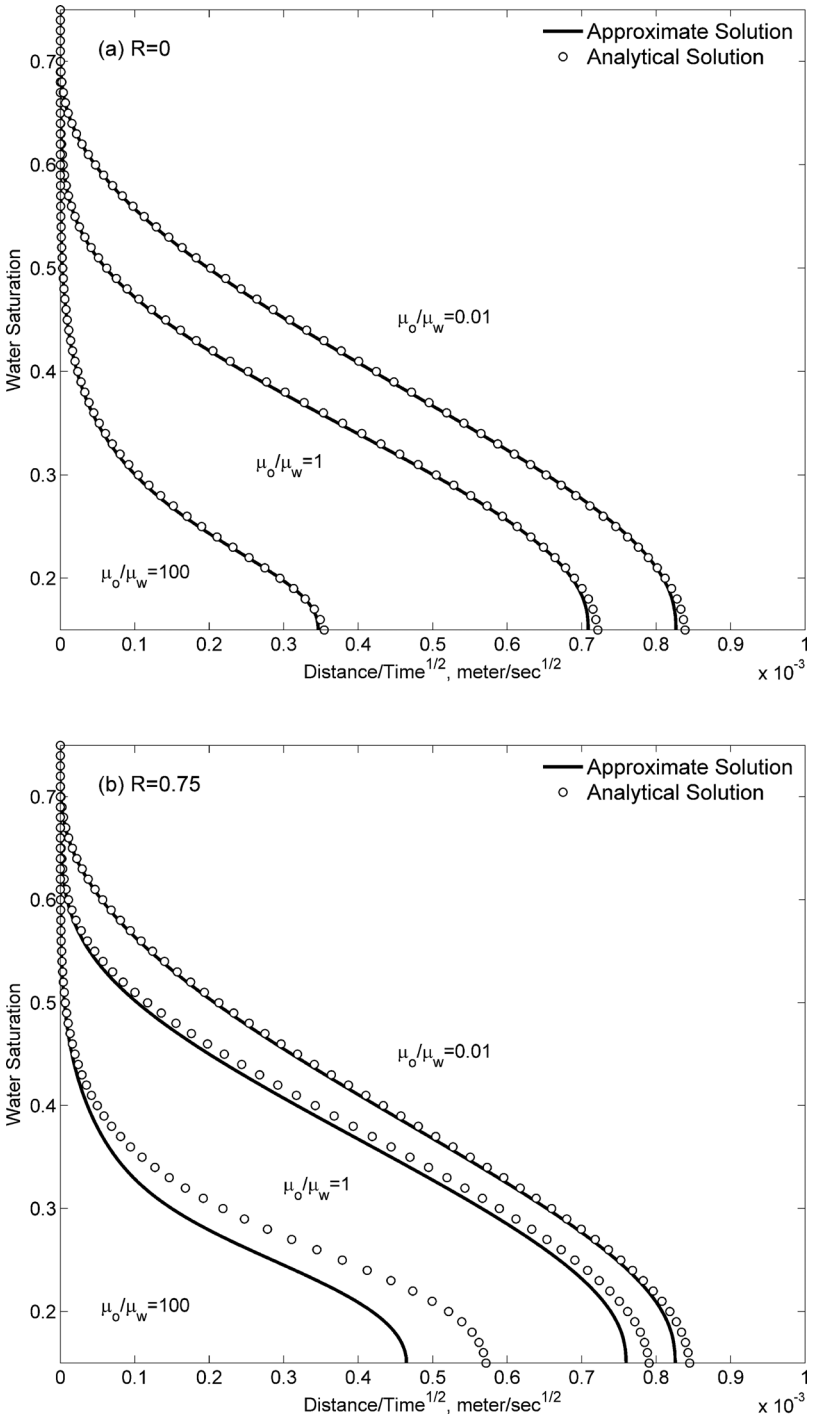

Figure 19. Comparison between analytical and approximate solutions for (a) $R = 0$, and (b) $R = 0.75$ at different viscosity ratios.

As mentioned previously, a conventional finite-difference formulation with an IMPES flow solver is used for the numerical computations (Appendix A). To ensure both accuracy and stability of the numerical solution, an automatic time-step approach that depends on the rate of change in pressures and saturations is adapted [*Aziz and Settari*, 1979]. This is achieved by restricting the maximum change of water saturation and oil pressure within a grid-cell to certain values; these in our simulations were selected to be 1.5% and 6.9×10^4 Pa, respectively. With this approach, the time-step size will consequently depend on the grid-cell size; as the grid-cell size decreases the time-step size will also decrease. This eventually makes the error norms presented in Figure 18 not solely a function of grid-cells, but also dependent on time-step size as well.

Table 2. Error L_1 in S_w Between Analytical and Approximate Solutions for Different Viscosity Ratios and R Values

$\mu_o/\mu_w\vert_{\mu_w=1}$	$R = 0$ (%)	$R = 0.25$ (%)	$R = 0.50$ (%)	$R = 0.75$ (%)	$R = 1$ (%)
0.01	0.2468	0.2537	0.2706	0.2777	
1.00	0.2101	0.2528	0.3677	0.9453	
100	0.2375	0.4689	1.1446	1.2001	

5.4. Comparison Between Analytical and Approximate Solutions

Using the approximate solution in equations (48) and (49), comparison is made with the analytical solutions for counter and cocurrent flow. The difference in S_w is demonstrated graphically in Figure 19 for different viscosity ratios and R values. The errors for the computed curves are summarized in Table 2 by varying viscosity ratios while fixing the other saturation-dependent properties. The calculation of the error is performed using equation (54) for $j = 1$. It is observed that the approximate solution performs very well for countercurrent flow ($R = 0$). It then starts to deviate as the value of R increases at high oil-to-water viscosity ratios. Nevertheless, the computed error values indicate acceptable estimates for relatively high R and viscosity ratios. On the other hand, the approximate solution gives very poor estimates compared to the analytical solution for $R = 1$. This could be improved, however, by adding more terms from the series and using other techniques to accelerate the convergence. At any rate, we are less interested in this range since unidirectional cocurrent flows may not be a common flow mechanism in natural flow systems.

6. Conclusions

Spontaneous imbibition proceeds by three main flow mechanisms: cocurrent, countercurrent, and cocurrent with some degree of countercurrent. Most analytical solutions previously introduced were developed to model the first two flow mechanisms. In this study, we show a new method to obtain semianalytically a solution for the third displacement process. This flow mechanism is explained by demonstrating the impact of the system length on cocurrent flow. This is achieved by capturing the effect of the boundary conditions in the analytical solutions by adjusting the amount of countercurrent flow in the system (adjusting the R value; the ratio of co to countercurrent flow). It is observed that there will be a critical saturation that can be identified from fractional flow curves and used to distinguish regions of co and countercurrent flow. This critical saturation changes as the saturation front moves into the rock. In addition, the water imbibition rate is not inversely proportional to $\sqrt{t}$ for such systems. This results in having multiple imbibition rate-functions during cocurrent displacements.

The variable imbibition rate functions are treated by the principle of superposition. This allows the breakdown of the problem into smaller parts, in which the fixed-R solution is considered valid. The final solution turns into a form that involves solving a convolution sum with arbitrary number of steps. The use of the principle of superposition may be justified in this case by the calculation of the distance along a fixed saturation path. From a practical point of view, the fixed-R solution provides a good approximation to the true solution. Moreover, if convolution sums are used, very close results are obtained for a few number of steps, even though this is still an approximate solution. From the relationship between the R values and time, it is indicated that the system starts mainly as countercurrent flow. The degree of cocurrent flow then increases sharply with time. Countercurrent flow remains for all time since capillary back pressure is neglected in present calculations. Nevertheless, this assumption can be relaxed by redefining pressure boundary conditions across the system and developing another expression for the R value. This is a topic for future work. We also present an empirical expression to accurately capture the evolution of R with time, which might be used in future studies to simplify the solution even further.

Using a perturbative approach, a new approximate solution is derived. The key concept is to convert the original nonlinear ordinary differential equation into an infinite sequence of simple equations that can be easily solved. This enables the calculation of the fractional flow function without the need to solve the implicit integral equations. Although the calculations can be carried out to arbitrary accuracy, an excellent match is obtained for countercurrent flow from the first three terms of the solution. As the amount of cocurrent flow increases during the displacement, the solution becomes less accurate. This method is easier to implement as compared with the implicit integral approach, since iterations are performed only on a single-point; the imbibition rate parameter.

In addition, a numerical comparison is presented, in which a traditional finite-difference formulation with IMPES solver is used. Unlike the well-known Buckley-Leverett solution for viscous-dominated displacements where injection rate is fixed and used as input in the numerical solutions, the water imbibition rate in capillary-driven flow is estimated from the numerical simulation. Convergence analysis is performed by computing error norms for water saturation and pressure profiles, as well as water imbibition rates. The order of convergence is about one for water saturation and imbibition rates, while approximately half of that rate of convergence is observed for pressure. This is possibly due to that flux and the evolution of saturation are related to the gradient of pressure and not the absolute value itself. In a numerical implementation, therefore, the pressure may converge slowly, even if the flow rates are captured accurately.

Appendix A: Numerical Simulation

We use for our numerical computations a conventional finite-difference formulation that uses an IMPES (Implicit Pressure Explicit Saturation) solver. A two-point flux approximation is employed with upstream-weighting of saturation-dependent functions in the phase flux calculations while average fluid saturations are used in the total flux equation [*Aziz and Settari*, 1979].

For every node, i connected to a number of neighbor nodes N_j having the index j, the total volumetric flow rate, $Q_{t_{ij}}=0$, for incompressible flow is zero, that is

$$\sum_j Q_{t_{ij}}=0\,, \tag{A1}$$

where $Q_{t_{ij}}$ is the summation of the individual phase rates, given by

$$\sum_j \left(Q_{o_{ij}}+Q_{w_{ij}}\right)=0\,. \tag{A2}$$

The individual phase rate is defined from Darcy's law, neglecting the effect of gravity, as follows:

$$Q_{f_{ij}}=\frac{k_{ij}A_{c_{ij}}}{\Delta x_{ij}}\frac{k_{rf_{ij}}}{\mu_f}\left(p_{f_i}-p_{f_j}\right)\qquad f=o,w\,. \tag{A3}$$

By combining equations (A2) and (A3), we have

$$\sum_j \frac{k_{ij}A_{c_{ij}}}{\Delta x_{ij}}\left(\frac{k_{ro}}{\mu_o}+\frac{k_{rw}}{\mu_w}\right)^n_{ij}\left[\left(p^{n+1}_{o_i}-p^{n+1}_{o_j}\right)-f^n_{w_{ij}}\left(p^n_{c_i}-p^n_{c_j}\right)\right]=0\,. \tag{A4}$$

The linear system of equations, equation (A4), solves for oil pressures p_o implicitly in all nodes. The saturation-dependent functions k_{ro}, k_{rw}, and f_w are evaluated at average water saturations at the previous time level n. Water saturations are then updated at the new time level $n+1$ using the following equation:

$$S^{n+1}_{w_i}=S^n_{w_i}+\frac{\Delta t}{V_{p_i}}\sum_j \frac{k_{ij}A_{c_{ij}}}{\Delta x_{ij}}\left(\frac{k_{ro}}{\mu_o}\right)^n_{ij}\left(p^{n+1}_{o_i}-p^{n+1}_{o_j}\right)\,, \tag{A5}$$

where V_p is the pore volume, A_c is the cross-sectional area to flow, and Δx is the length between two nodes. In this study, Δx is set to a fixed value.

Since an IMPES solver is used, the selection of time step size Δt is crucial for the stability of the numerical solutions. We use an automatic time stepping approach that depends on a maximum water saturation and oil pressure change S_{max} within a grid cell. This is achieved in two steps. First, we calculate time-step sizes based on a pre-set maximum saturation change for all cells; according to the following formula:

$$\Delta t=\frac{S_{\max}}{\max\left|\frac{\sum_j Q_{o_{ij}}}{V_{p_i}}\right|}\,. \tag{A6}$$

Using this (current) time-step size, oil pressures are calculated at the new time-level and subtracted from the values obtained at the previous time step. If the pressure difference is larger than a preset error tolerance, the current time-step size is reduced and computations are repeated until convergence. In our simulation, the maximum change in water saturation and oil pressure within a time-step was set to 1.5% and 6.9×10^4 Pa, respectively.

Appendix B: Mathematical Derivation of Oil-Phase Pressure Function

Starting from Darcy's law for the oil phase;

$$q_o = -\frac{kk_{ro}}{\mu_o}\frac{\partial p_o}{\partial x}\,. \tag{B1}$$

Integrating equation (B1) with respect to x, after few arrangements, yields

$$\int_{p_o(x=0)}^{p_o(x)} \mathrm{d}p_o = -\frac{\mu_o}{k}\int_{x=0}^{x}\frac{q_o(\beta)}{k_{ro}(\beta)}\mathrm{d}\beta\,. \tag{B2}$$

Since $q_o(x)=q_t-q_w(x)$, equation (B2) becomes

$$p_o(x)-p_o(0) = -\frac{\mu_o}{k}\int_0^x \frac{q_t-q_w(\beta)}{k_{ro}(\beta)}\mathrm{d}\beta\,. \tag{B3}$$

In addition, $q_t = R\,q_{x0}$, and $q_w(x)=q_{x0}\,F_w(x)$;

$$p_o(x)-p_o(0) = -\frac{\mu_o\,q_{x0}}{k}\int_0^x \frac{R-F_w(\beta)}{k_{ro}(\beta)}\mathrm{d}\beta\,. \tag{B4}$$

Substituting $q_{x0}=\frac{A}{\sqrt{t}}$;

$$p_o(x)-p_o(0) = -\frac{\mu_o}{k}\frac{A}{\sqrt{t}}\int_0^x \frac{R-F_w(\beta)}{k_{ro}(\beta)}\mathrm{d}\beta\,. \tag{B5}$$

Appendix C: Mathematical Derivations for the Approximate Solutions

We show here the detailed derivations of the solutions for equation (33) only, which is exactly similar to equations (34) and (35). The differential equation is given by

$$F''_0 = \frac{-\omega D}{(1-f_n)}, \qquad F_0(S_i)=0,\; F_0(S_{x0})=1\,. \tag{C1}$$

By double-integrating equation (C1), we get

$$F_0 = -\omega\int_{S_w}^{S_{x0}}\mathrm{d}\beta\int_{\beta}^{S_{x0}}\frac{D(\alpha)}{1-f_n(\alpha)}\mathrm{d}\alpha + c_1 S_w + c_2\,. \tag{C2}$$

Let us introduce the following function:

$$T_0(S_w) = \int_{S_w}^{S_{x0}}\mathrm{d}\beta\int_{\beta}^{S_{x0}}\frac{D(\alpha)}{1-f_n(\alpha)}\mathrm{d}\alpha\,. \tag{C3}$$

Integrating equation (C3) by parts;

$$T_0(S_w) = -S_w\int_{S_w}^{S_{x0}}\frac{D(\beta)}{1-f_n(\beta)}\mathrm{d}\beta + \int_{S_w}^{S_{x0}}\frac{\beta\,D(\beta)}{1-f_n(\beta)}\mathrm{d}\beta\,, \tag{C4}$$

$$T_0(S_w) = \int_{S_w}^{S_{x0}}\frac{(\beta-S_w)D(\beta)}{1-f_n(\beta)}\mathrm{d}\beta\,. \tag{C5}$$

Equation (C2) can then be written as

$$F_0 = -\omega T_0(S_w) + c_1 S_w + c_2\,. \tag{C6}$$

The constants c_1 and c_2 in equation (C6) are found by using the boundary conditions, which gives the following equations for c_1 and c_2:

$$1 = c_1 S_{x0} + c_2 \,, \tag{C7}$$

$$0 = -\omega T_0(S_i) + c_1 S_i + c_2 \,. \tag{C8}$$

Solving for c_1 and c_2;

$$c_1 = \frac{1-\omega T_0(S_i)}{S_{x0}-S_i} \,, \tag{C9}$$

$$c_2 = \omega T_0(S_i) - \left(\frac{1-\omega T_0(S_i)}{S_{x0}-S_i}\right) S_i \,. \tag{C10}$$

Substituting back into equation (C6);

$$F_0 = -\omega T_0(S_w) + \left(\frac{1-\omega T_0(S_i)}{S_{x0}-S_i}\right) S_w + \omega T_0(S_i) - \left(\frac{1-\omega T_0(S_i)}{S_{x0}-S_i}\right) S_i \,, \tag{C11}$$

$$F_0 = -\omega T_0(S_w) + \left(\frac{S_w-S_i}{S_{x0}-S_i}\right) - \omega T_0(S_i)\left(\frac{S_w-S_i}{S_{x0}-S_i}\right) + \omega T_0(S_i) \,. \tag{C12}$$

After a few algebraic manipulations;

$$F_0 = S_n(S_w) - \omega(T_0(S_w) - T_0(S_i)(1-S_n(S_w))) \,, \tag{C13}$$

where

$$S_n(S_w) = \frac{S_w-S_i}{S_{x0}-S_i} \,. \tag{C14}$$

Similar procedures are applied for the other differential equations.

Notation

A	imbibition rate parameter, m/$\sqrt{t}$.
A_c	cross-sectional area, m^2.
D	capillary-dispersion function, m^2/s.
f_i	the function f_w evaluated at S_i, fraction.
f_n	normalized fraction flow, defined in equation (12), fraction.
f_w	viscous-dominated fraction flow function, fraction.
F_w	fractional flow function that includes capillary effects, fraction.
$F_{0,1,2,n}$	fraction flow of zeroth, first, second, and nth orders in the perturbation series.
$G_{0,1,2,n}$	integral functions defined in the approximate solutions.
H	height of the synthetic reservoir model, m.
i	multiple purpose, defined as it appears in the text.
j	multiple purpose, defined as it appears in the text.
k	absolute permeability, m^2.
k_{ro}	oil relative permeability, fraction.
k_{rw}	water relative permeability, fraction.
$\bar{k}_{ro}$	oil relative permeability at initial water saturation, fraction.
$\bar{k}_{rw}$	water relative permeability at residual oil saturation, fraction.
L	length of linear system, m.
L_j	error norms.
n	multiple purpose, defined as it appears in the text.
n_c	exponent in the power-law model of capillary pressure model.
n_o	exponent in the power-law model of oil relative permeability model.
n_w	exponent in the power-law model of water relative permeability model.
$n+1$	new time-level.

p_c	capillary pressure function, Pa.
p_o	oil-phase pressure, Pa.
$\bar{p}_c$	maximum capillary pressure at the irreducible water saturation.
q_t	total flux, m/s.
q_w	Water flux, m/s.
q_{x0}	water flux at inlet boundary at $x = 0$, m/s.
Q_o	oil volumetric flow rate, m^3/s.
Q_t	total volumetric flow rate, m^3/s.
Q_w	water volumetric flow rate, m^3/s.
R	the ratio of the total flux to the water at the inlet, fraction.
R_0	R at $t = 0$, which is always equal to 0.
R_τ	R as a function of t, used in the convolution sums.
S_i	initial water saturation, fraction.
S_{max}	maximum water saturation change in a grid-cell, fraction.
S_n	normalized water saturation, fraction.
S_{orw}	residual oil saturation, fraction.
S_w	water saturation, fraction.
S_{wir}	irreducible water saturation, fraction.
S_{x0}	water saturation at the inlet boundary at $x = 0$, fraction.
S^*	critical water saturation defining co from countercurrent flow regions.
t	time, s.
$T_{0,1,2,n}$	integral functions defined in the approximate solutions.
V_p	pore volume, m^3.
W	width of the synthetic reservoir model, m.
x	distance, m.
x_f	position of the front, m.
Y	special function defined in equation (23).
β	dummy variable of integration.
ϕ	porosity, fraction.
μ_w	water viscosity, mPa.s.
μ_o	oil viscosity, mPa.s.
Δt	time step size, s.
Δx	grid cell size, m.
τ	dummy variable of integration.
δ	perturbation parameter.
ω	a constant used in the perturbative approximation, defined in equation (30).
λ	variable of transformation.

Acknowledgments
The first author would like to thank Saudi Aramco for the generous, financial support toward his PhD at Imperial College London. All data presented in this paper are available from the authors upon request (hasan.a.nooruddin@gmail.com).

References

Agada, S., and S. Geiger (2013), Optimising gas injection in carbonate reservoirs using high-resolution outcrop analogue models, in *SPE Reservoir Characterization and Simulation Conference and Exhibition*, Soc. of Pet. Eng., Abu Dhabi, UAE.

Aziz, K., and A. Settari (1979), *Petroleum Reservoir Simulation*, Chapman and Hall, Applied Science Publishers Ltd., London, U. K.

Bender, C. M., and S. A. Orszag (1999), *Advanced Mathematical Methods for Scientists and Engineers I*, Springer-Verlag, N. Y.

Bender, C. M., K. A. Milton, S. S. Pinsky, and L. Simmons Jr. (1989), A new perturbative approach to nonlinear problems, *J. Math. Phys.*, *30*(7), 1447–1455.

Beydoun, Z. R. (1998), Arabian plate oil and gas: Why so rich and so prolific?, *Episodes*, *21*(2), 74–81.

Bjørnarå, T. I., and S. A. Mathias (2013), A pseudospectral approach to the McWhorter and Sunada equation for two-phase flow in porous media with capillary pressure, *Comput. Geosci.*, *17*(6), 889–897.

Chen, Z.-X., et al. (1988), Some invariant solutions to two-phase fluid displacement problems including capillary effect (includes associated papers 18744 and 19037), *SPE Reservoir Eng.*, *3*(2), 691–700.

Chen, Z.-X., G. Bodvarsson, and P. Witherspoon (1992), Comment on exact integral solutions for two-phase flow by David b. McWhorter and Daniel k. Sunada, *Water Resour. Res.*, *28*(5), 1477–1478.

Fokas, A., and Y. Yortsos (1982), On the exactly solvable equation s_t=(βs+γ)^-2s_x_x+α(βs+γ)^- 2s_x occurring in two-phase flow in porous media, *SIAM J. Appl. Math.*, *42*(2), 318–332.

Fučík, R., J. Mikyška, M. Beneš, and T. H. Illangasekare (2007), An improved semi-analytical solution for verification of numerical models of two-phase flow in porous media, *Vadose Zone J.*, *6*(1), 93–104.

Haugen, Å., M. Fernø, G. Mason, and N. Morrow (2014), Capillary pressure and relative permeability estimated from a single spontaneous imbibition test, *J. Pet. Sci. Eng.*, *115*, 66–77.

Kashchiev, D., and A. Firoozabadi (2003), Analytical solutions for 1d countercurrent imbibition in water-wet media, *SPE J.*, *8*(4), 401–408.
Mason, G., and N. R. Morrow (2013), Developments in spontaneous imbibition and possibilities for future work, *J. Pet. Sci. Eng.*, *110*, 268–293.
McWhorter, D. B., and D. K. Sunada (1990), Exact integral solutions for two-phase flow, *Water Resour. Res.*, *26*(3), 399–413.
McWhorter, D. B. (1971), Infiltration affected by flow of air, *Hydrol. Pap., 49*, Colo. State Univ., Fort Collins, Colo.
Montaron, B. (2008), Carbonate evolution, in *Oil and Gas Middle East*, pp. 26–31, ITP Publishing Group Ltd., Dubai, UAE.
Morrow, N. R., and G. Mason (2001), Recovery of oil by spontaneous imbibition, *Curr. Opin. Colloid Interface Sci.*, *6*(4), 321–337.
Mou, J., S. Zhang, and Y. Zhang (2012), Acid leakoff mechanism in acid fracturing of naturally fractured carbonate oil reservoirs, *Transp. Porous Media*, *91*(2), 573–584.
Ruth, D. W., G. Mason, M. A. Fernø, Å. Haugen, N. R. Morrow, and R. Arabjamaloei (2015), Numerical simulation of combined co-current/counter-current spontaneous imbibition, in *International Symposium of the Society of Core Analysts*, St. John's Newfoundland and Labrador, Canada, pp. 16–21.
Schmid, K., S. Geiger, and K. Sorbie (2011), Semianalytical solutions for cocurrent and countercurrent imbibition and dispersion of solutes in immiscible two-phase flow, *Water Resour. Res.*, *47*, W02550, doi:10.1029/2010WR009686.